

¹ Validation of Ozone Monitoring Instrument Nitrogen ² Dioxide Columns

E. A. Celarier,¹ E. J. Brinksma,² J. F. Gleason,³ J. P. Veefkind,² A. Cede,⁴

J. R. Herman,³ D. Ionov,^{5,6} F. Goutail,⁶ J-P. Pommereau,⁶ J-C. Lambert,⁷

M. van Roozendael,⁷ G. Pinardi,⁷ F. Wittrock,¹¹ A. Schönhardt,¹¹

A. Richter,¹¹ O. W. Ibrahim,¹³ T. Wagner,¹² B. Bojkov,⁴ G. Mount,⁸

E. Spinei,⁸ C. M. Chen,⁹ T. J. Pongetti,⁹ S. P. Sander,⁹ E. J. Bucsela,⁴

M. O. Wenig,⁴ D. P. J. Swart,¹⁰ H. Volten,^{2,10} M. Kroon,² and P. F. Levelt²

Edward A. Celarier, SGT, Inc. 7701 Greenbelt Rd, Greenbelt, MD 20770 (Edward.Celarier@gsfc.nasa.gov)

Ellen Brinksma, KNMI, 3730 AE De Bilt, The Netherlands (ellen.brinksma@knmi.nl)

¹SGT, Inc., 7701 Greenbelt Rd Ste 400,

3 **Abstract.** We review the nitrogen dioxide (NO₂) data product, which
4 is based on measurements made in the spectral region 415–465 nm by the
5 Ozone Monitoring Instrument (OMI) on the EOS-Aura Satellite. A number
6 of ground- and aircraft-based measurements have been used to validate the
7 data product’s three principal quantities: stratospheric, tropospheric, and
8 total NO₂ column densities. It is found that OMI overestimates the strato-
9 spheric column by about 10%, and underestimates both the total and tro-
10 pospheric columns by 15 – 30%. Because some of the techniques have not
11 themselves been validated, and because of problems inherent in comparing
12 point measurements from the ground to large area averaged satellite mea-
13 surements, and because some of the measurements have been made only over
14 short periods of time, validation results are sometimes only qualitative.

Greenbelt MD 20770, USA.

1. Introduction

15 The Ozone Monitoring Instrument (OMI) is a space borne spectroradiometer that uses
16 a 2-dimensional CCD array detector to simultaneously measure the spectra of the earth
17 shine radiance at large number of viewing angles, approximately transverse to the Aura
18 spacecraft's flight track. OMI measures in three broad spectral regions (UV-1, UV-2, and
19 VIS), with a spectral resolution on the order of 0.5 nm. Applying spectral fitting techniques
20 to the OMI data permits the simultaneous retrieval of a wide range of atmospheric trace
21 gas concentrations as well as cloud and aerosol properties and loadings. Among the trace
22 gases that can be retrieved, ozone (O_3) and nitrogen dioxide are identified as essential
23 measurements, both for the ongoing monitoring of the Earth's stratospheric ozone layer
24 and for the monitoring of tropospheric air quality. A more extensive discussion of the OMI
25 instrument itself can be found in *Levelt and Bhartia* [2007].

26 The OMI NO_2 data production algorithm is designed to retrieve total vertical column
27 densities of NO_2 and separate stratospheric and tropospheric column densities; this en-
28 ables the improvement in the calculation of the total vertical column. The stratosphere-
29 troposphere separation is achieved using a low-pass spatial filtering technique; the small-
30 gradient portion of the initial estimate of the total NO_2 field is identified as the background
31 stratospheric field. Measurements that exceed the constructed stratospheric field are taken
32 to indicate significant tropospheric pollution. This separation is important (and possible)
33 because the chemistry and dynamics of NO_2 are different between the stratosphere and

²Royal Netherlands Meteorological

34 the troposphere. Accurate measurements of the tropospheric NO₂ are significant for the
35 characterization of air quality, a primary objective of the Aura and OMI missions.

36 A number of efforts toward NO₂ validation have been initiated, in which measurements
37 are made coincident with OMI overpass measurements. The purpose of this paper is to
38 provide an overview of results from these efforts. A variety of instruments and techniques
39 have been used, each with its characteristic sensitivity to stratospheric, tropospheric,
40 or total column NO₂. This paper will address the advantages and, in some cases, the
41 limitations of the various measurements.

42 Several of the techniques described are new, and have not been well-validated. In addi-
43 tion, there is an essential difference between observations of NO₂ taken from the ground,
44 and observations averaged over a satellite field of view (FOV). Spatial inhomogeneity,
45 characteristic of airborne constituents emitted at (possibly moving) point sources, and
46 subject to surface-level winds, implies that a single point measurement will often not be a
47 representative sample within a “collocated” a satellite FOV covering a region of the order
48 of several hundred square kilometers. Monthly average comparisons of ground-based and
49 satellite measurements can remove much of the variability due to FOV-point measurement
50 differences. A preliminary measurement of horizontal inhomogeneity in the NO₂ field is
51 presented in the DANDELIONS overview paper [*Brinkma et al.*, 2007], using a set of si-
52 multaneous tropospheric NO₂ measurements made at different azimuths. *Veefkind et al.*
53 [2007] show a comparison of regridDED OMI NO₂ data with ground-based observations by
54 the Dutch national air quality network. This network distinguishes regional stations, and
55 city and street stations, which are close to source regions. For the period of the satellite

Institute, 3730 AE De Bilt, The

56 data, NO₂ reported by 35 stations around the Netherlands, averaged between 11:00 and
57 14:00 h local time, was compared to the collocated OMI measurements. A strong correla-
58 tion ($R = 0.94$) between the satellite data and the regional station data was found. By
59 contrast, correlations with urban stations are weak, because local conditions may vary
60 strongly over a few hundred meters, far smaller than the spatial resolution of OMI. Be-
61 cause of both the novelty of some of the techniques, and such spatial-scale effects, specific
62 results are sometimes limited to qualitative, or order-of-magnitude, conclusions.

63 Among the validation studies discussed here are ground based observations made within
64 the SAOZ and DOAS networks. These are zenith-sky, twilight measurements, which are
65 sensitive to the stratospheric NO₂ column (as explained in section 4.1.1). In addition,
66 the locations are very often pristine areas, or at elevation. Even if the instrumentation
67 were sensitive to tropospheric NO₂, the lack of pollution would lead to measurements
68 dominated by the stratospheric NO₂ amount.

69 To focus on polluted areas, where satellite NO₂ retrievals are most challenging, novel,
70 or as yet unvalidated techniques must be used.

71 Measurements of scattered light by the MultiAxial DOAS (MAX-DOAS) technique, using
72 a range of viewing angles, from nearly horizontal through zenith, are sensitive to the
73 tropospheric part of the column, and provide both total and tropospheric NO₂ amounts.
74 We present results from MAX-DOAS measurements taken in a polluted area, but away from
75 immediate local sources, in section 4.2.1.

76 Direct-sun ground based measurements, made with a Brewer spectrophotometer
77 and with newly-developed direct-sun instruments, including a high-resolution Fourier-

Netherlands.

78 transform UV-FTS technique, and a number of direct-sun DOAS-type measurements, are
79 sensitive to the total NO₂ column. We will briefly review some preliminary results from
80 these methods in section 4.3.

81 Validation of the OMI NO₂ data should take account of the sensitivity of the numerous
82 geophysical and geometric algorithmic inputs. These include the *a priori* profile shapes,
83 surface albedo, and measured and assumed cloud properties. These, in particular, greatly
84 affect the air mass factors (AMF; the ratio of slant-column density of the absorber along
85 the optical path to the vertical column density) the algorithm calculates. Tropospheric
86 NO₂ profiles have been measured with lidar in the Netherlands, during a number of days in
87 September 2006, and with airborne instrumentation during various validation campaigns.

88 During the Polar Aura Validation Experiment (PAVE) (flights from New Hampshire,
89 January and February 2005) the TD-LIF instrument [*Thornton et al., 2000; Cleary et al.,*
90 2002] was used for *in situ* sampling of NO₂, during the aircraft flights. The NASA DC-8
91 performed two flight legs at 300 m altitude, near the top of the boundary layer. When
92 flights entered the boundary layer, strongly enhanced concentrations of NO₂ were found.

93 During the INTEX-B campaign (flights from Houston, Texas, March 2006 and from
94 Honolulu, Hawaii, and Anchorage, Alaska, April and May 2006) the TD-LIF instrument

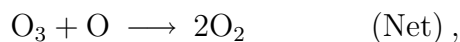
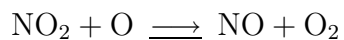
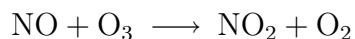
³Code 613.3, NASA Goddard Space

95 measured NO_2 *in situ*. Spirals were flown by the NASA DC-8 during several flights in
96 spatial and temporal collocation with OMI observations.

97 Besides INTEX-B, a small number of other airborne campaigns have been carried out,
98 measuring NO_2 *in situ*, and have been applied to satellite validation [*Heland et al.*, 2002;
99 *Martin et al.*, 2006].

1.1. Nitrogen dioxide in the stratosphere

100 Nitrogen dioxide participates both directly and indirectly in the catalytic destruction
101 of ozone in the stratosphere. Direct ozone destruction occurs *via* the reactions



102 while NO_2 concentrations indirectly control ozone loss through other catalytic cycles by
103 controlling, for example, the distribution of chlorine between its catalytically active (ClO)
104 and inactive, reservoir (ClONO₂) species:



105 In the stratosphere, NO_2 concentration has a distinctive diurnal cycle that is dependent
106 on the reactions shown in Figure 1. At night, all the photolysis reactions stop, shifting
107 the steady state to NO_2 . NO_2 is converted, through ozonolysis, to NO_3 , which can further
108 combine with NO_2 to form N_2O_5 . This results in a slow decrease of NO_2 over the course of
109 the night. When the air is again sunlit, the N_2O_5 rapidly redissociates to NO_2 and NO_3 ,

Flight Center, Greenbelt MD 20771, USA.

110 which photolyzes instantaneously, mostly to NO. Meanwhile, NO₂ photolyzes very rapidly,
111 and so decreases very rapidly at sunrise. While in daylight, the dominant processes are
112 the interconversion between NO and NO₂. There are a number of specific mechanistic
113 pathways that can contribute to this interconversion. The most typical atmospheric states
114 (conditions of temperature and ozone concentration, latitude, and season) lead to a slow
115 increase in NO₂ concentration over the course of the daylight hours. At sunset, the
116 photolysis reactions again switch off, and the NO₂ concentration rises rapidly. In addition
117 to the chemical and photochemical processes, transport by the winds, particularly in
118 the vicinity of the polar jets may mean that the air that one is measuring has not had
119 the photochemical history one would expect, based on location and local time, alone.
120 Some caution is therefore needed in matching satellite measurements to the ground based
121 measurements.

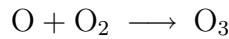
122 The time-dependence of the stratospheric NO₂ concentration has important implica-
123 tions for the validation of the space based NO₂ measurements. If the ground based
124 measurements are not collocated in time with the OMI measurements, they need to be
125 corrected, using photochemical and transport models, to account for the time difference.
126 In addition, if the ground-based measurements entail an optical path that is more hor-

⁴GEST Program, University of Maryland

127 izontal than vertical, view and solar geometries must be taken into consideration when
128 identifying “collocated” measurements.

1.2. Nitrogen dioxide in the troposphere

129 In the troposphere, nitrogen oxides are a significant contributor to poor air quality.
130 Both NO and NO₂ are harmful to lung tissue, and, as a powerful oxidizing agent, NO₂
131 is harmful to biological tissue generally. Besides its direct effects, photolysis of NO₂
132 contributes to ozone production according to



133 Nitrogen oxides are produced in high-temperature processes in the atmosphere, most
134 notably in combustion (fossil fuels and biomass burning) and in lightning. Nearly all
135 the NO_x (NO + NO₂) that is significant for human health is produced by industrial and
136 urban activity, including transportation and power generation. As a rule, the higher the
137 combustion temperature, the more NO_x is produced; the primary reactions necessary for
138 NO_x production are the thermolysis of N₂ and O₂. The most common species directly
139 formed in combustion is NO, however NO readily oxidizes in air to NO₂:



140 Gaseous NO₂ is red in color, and gives rise to the characteristic brownish cast of polluted
141 air. NO₂ is removed through conversion to HNO₃, nitric acid, which readily dissolves in
142 any available water droplets. NO₂ plumes are detected only up to about 100 km from

Baltimore County, Baltimore MD, USA.

143 their industrial or urban source. In the neighborhood of industrial or urban sources, there
144 is a distinct diurnal pattern in the production and loss of NO_x. The diurnal signal at any
145 location, particularly in the boundary layer, is the result of a complex interplay between
146 the emission source field in space and time, photochemical effects, advection by boundary
147 layer winds, and the concentrations of chemical sinks for NO_x species. As mentioned
148 before, these also give rise to spatial inhomogeneities on a sub-100 m scale. At mid- to
149 low-latitudes, where a polar-orbiting satellite passes over a given location is only once or
150 twice a day, the satellite only sees a “snapshot” of the state of the polluted atmosphere at
151 the overpass times. In the mid-to-upper latitudes, inconsistent measurements, from one
152 orbit to the next, over some location may well result from significant changes in the NO₂
153 concentrations over the intervening 100 minutes, as well as from other rapid geophysical
154 changes, e.g. in cloud cover.

1.3. OMI measurement of NO₂

155 The Aura satellite is a polar-orbiting, sun-synchronous satellite, whose orbital period
156 is 99 minutes. Aura flies over the entire surface of the Earth every 14–15 orbits. Using
157 the 2-dimensional CCD array detector, with pixel binning factors chosen to optimize the
158 signal-to-noise ratio, the instrument measures earthshine radiance spectra simultaneously
159 in 60 effective fields of view (FOV), approximately transverse to the flight track, every 2
160 seconds (the CCD is read out every 0.4 s, and co-added in groups of 5), over a range of
161 angles 57° either side of nadir. This gives a sufficient “push-broom” width to view the

⁵Department of Atmospheric Physics,

162 entire sunlit surface of the Earth, even in the tropics, with multiple orbital overlaps for
163 much of the mid- to high-latitude regions.

164 During normal operations, OMI measures the solar irradiance spectrum once every 24
165 hours. The ratio of the earthshine radiance to solar irradiance, the *spectral albedo*, is
166 calculated for each FOV. The OMI NO₂ algorithm starts by fitting the spectral albedo to
167 a set of reference spectra to get slant column densities (SCD). A simple air mas factor
168 (AMF), calculated based on the assumption of unpolluted conditions, where most of the
169 NO₂ is in the stratosphere, is used to obtain an initial vertical column density (VCD). The
170 data from up to 15 consecutive orbits are assembled and analyzed in order to construct a
171 “background” field (essentially, the unpolluted, stratospheric field, with a small contribu-
172 tion from the upper troposphere). The individual FOV initial VCDs are compared to the
173 background field, and where they exceed the background field, significant tropospheric
174 pollution is inferred. The VCDs are then recalculated, using an AMF derived using an *a*
175 *priori*, model-derived tropospheric NO₂ profile shape. This is used to recalculate the total
176 column, and hence the tropospheric column.

1.4. Data availability

177 The OMI NO₂ data product is available in a number of different geospatial forms:

- 178 • Level 2 orbital swath (L2);
- 179 • Daily global gridded, 0.25° × 0.25° (L2G);
- 180 • Station and regional overpass (OVP).

Research Institute of Physics, St.

181 The L2 and L2G datasets and associated documentation are freely available through the
182 NASA Goddard Earth Sciences Data and Information Services Center (GES-DISC, URL:
183 <http://daac.gsfc.nasa.gov/Aura/OMI/index.shtml>).

184 The OVP data, generated on a daily basis for over 100 locations around the world and
185 also in support of validation and regional pollution studies, are available through the
186 Aura Validation Data Center (AVDC, URL: [http://avdc.gsfc.nasa.gov/Data/Aura/](http://avdc.gsfc.nasa.gov/Data/Aura/OMI/OMN02/index.html)
187 [OMI/OMN02/index.html](http://avdc.gsfc.nasa.gov/Data/Aura/OMI/OMN02/index.html)). The subsetted data used for this paper were generated at the
188 AVDC using the recommended usage quality flags [*Celarier et al.*, 2006].

189 Both the L2G and OVP data products are derived from the L2 data set, and not all
190 of the fields found in the L2 data may be found in the derived data products. The
191 L2 data are available as Hierarchical Data Format–Earth Observing System (HDF-EOS)
192 format files, which consist of three data groups: Geolocation Fields, Data Fields, and File
193 Attributes. Each data file has a corresponding metadata file; copies of all the metadata
194 are also included in the data file. The data fields include all the values of intermediate
195 variables calculated en route to the principal data fields. Complete details concerning the
196 contents of the Level 2 files are available in *Veeffkind and Celarier* [2006].

197 The L2G files are also HDF-EOS files, and contain a $0.25^\circ \times 0.25^\circ$ grid data structure.
198 Each cell of the grid contains a stack of data values for all the FOVs whose centers fell
199 within that cell. For each FOV a subset of the available L2 fields is stored. Because it is
200 organized geographically, the L2G data set should be suitable for users who wish to study

Petersburg State University, St. Petersburg,

201 specific geographic locations, as, for example, in the case of validation against ground
202 based measurements, or for regional air quality studies.

203 Field campaign data, and other ground-based measurement data are also available
204 through the AVDC.

205 Though all the data have been publicly released and are freely available, prospective
206 data users are strongly encouraged to contact the principal investigators responsible for
207 the data sets.

2. OMI Measurement

208 Atmospheric NO₂ column densities are retrieved using spectral measurements of the
209 solar irradiance and earth shine radiance in the wavelength region 415–465 nm, using
210 the instrument’s VIS detector. The measurements are made with a spectral resolution of
211 ~ 0.5 nm. Daily measurements of the solar irradiance have been made since the instru-
212 ment became operational, with the exception of the period 2006 February 28 through 2006
213 March 3, when a problem with the instrument’s folding mirror prevented making daily
214 irradiance measurements. Using measured irradiance spectra has resulted in the appear-
215 ance of stripe structure in virtually all the data products, in which the retrieved quantities
216 have different means at each of the 60 cross-track positions. This has necessitated the
217 implementation of “destriping” algorithms.

218 The OMI instrument design and performance have been described by *Levelt et al.*
219 [2006b, a]. *Dobber et al.* [2006] have discussed the calibration of the instrument, and
220 the origin of the striping, or cross-track bias.

Russia

3. OMI Algorithm

221 In this section we present the essential details of the algorithm. A much more detailed
222 description of the OMI NO₂ algorithm, and its theoretical underpinnings may be found in
223 [*Bucsela et al.*, 2006; *Boersma et al.*, 2002].

224 The OMI NO₂ algorithm proceeds in three steps. In the first step, spectral fitting (the
225 DOAS method) is used to fit the logarithm of the ratio of radiance to irradiance to a
226 set of laboratory-measured absorption spectra of the trace gases, plus a function that
227 models the effect of the rotational raman effect, plus a cubic polynomial to model the
228 wavelength dependence of Rayleigh and aerosol scattering. The coefficients thus obtained
229 give estimates of the slant column densities (SCD) of the various trace gases. To proceed
230 further, an initial estimate of the vertical column density (VCD; V_{init}) is made using an
231 AMF that is computed using a typical profile containing very little tropospheric NO₂. In
232 the second step, a number of candidate AMFs are computed, based on assumed NO₂ profile
233 shapes for polluted and unpolluted scenes, and for clear and cloudy conditions.

234 In the third step, data are assembled from each orbit and the orbits occurring within
235 ± 12 hours of it. Within 1° latitude bands a wave analysis (up to wave-2) is performed
236 on the V_{init} after masking data from known persistent strong NO₂ sources, as well as
237 any algorithmically-determined outliers. The resulting model is then taken to model
238 the unpolluted, or “background” field. The value of V_{init} for each field-of-view is then
239 compared to the background field. If it significantly exceeds the background field, then

⁶CNRS, Route des Gatines, 91370

240 the VCD is recomputed using an AMF that is computed assuming an NO₂ profile that has
241 substantial tropospheric concentration.

242 The following subsections provide more detail about these computations.

3.1. Slant column densities

243 The first part of the calculation of NO₂ columns consists in calculating the slant column
244 densities. Since the OMI-measured radiance and irradiance spectra, and the laboratory
245 spectra are all measured on different wavelength scales, the measured spectra are interpo-
246 lated onto a common scale. The spectral albedo, R , is then fit by a nonlinear least-squares
247 technique onto the function

$$R(\lambda) = P_3(\lambda) \cdot \exp(-c_{\text{NO}_2} \cdot \sigma_{\text{NO}_2}(\lambda) - c_{\text{O}_3} \cdot \sigma_{\text{O}_3}(\lambda)) \cdot \\ (1 + c_{\text{ring}} \cdot \sigma_{\text{ring}}(\lambda)) , \quad (3)$$

248 where σ is the absorption cross section of the indicated species, and P_3 is a third-order
249 polynomial in the wavelength, which models the component of the spectrum that is
250 smoothly varying, due to Rayleigh and Mie scattering. Literature spectra are used for
251 σ_{NO_2} [Vandaele *et al.*, 1998], σ_{O_3} [Burrows *et al.*, 1999], and σ_{ring} [Chance and Spurr,
252 1997]. These spectra were convolved with a model OMI instrument slit function prior to
253 use in the fitting algorithm. In all, each measured spectrum is subjected to a nonlin-
254 ear least-squares fit with a total of seven free parameters (c_{NO_2} , c_{O_3} , c_{ring} , and the four

Verrières le Buisson, France

255 coefficients in $P_3(\lambda)$). The algorithm also estimates the uncertainties in each of the fit
256 parameters, as well as the χ^2 error and R.M.S. error of the fit.

3.2. Initial vertical column densities

257 Initial estimates of the vertical column density (V_{init}) are calculated using AMFs derived
258 from typical climatological profile shapes, with a nominal amount of NO_2 assumed in
259 the troposphere (AMF_{init}). That is, the initial vertical columns are computed under the
260 assumption that the troposphere is not polluted.

3.3. Stratosphere-troposphere separation

261 At the core of the OMI NO_2 algorithm is a procedure to identify fields-of-view (FOV)
262 where there is significant tropospheric NO_2 . This is required because the air mass factor
263 depends upon the profile shape (though not the total amount, since the trace gas is op-
264 tically thin): FOVs where there is significant tropospheric NO_2 require a different AMF to
265 compute the VCD from the SCD. It is observed [*Gordley et al.*, 1996] that the stratospheric
266 NO_2 field has relatively small gradients, particularly in the zonal direction. Our procedure
267 for the stratosphere-troposphere separation essentially identifies the slowly-varying com-
268 ponent of the total NO_2 field as the stratospheric field, and the rest as the tropospheric
269 field.

270 Each orbit is treated as follows. The “target” orbit’s data are read in, along with the
271 data from all other available orbits that were measured within ± 12 hours of the target.
272 Each FOV is identified with a grid cell on a $1^\circ \times 1^\circ$ grid in latitude and longitude. For
273 all the FOVs that are identified with a particular grid cell, a “cost” is computed from

⁷Chemistry and Physics of Atmospheres,

274 the initial AMF and uncertainty estimate for the V_{init} ; the value of V_{init} having the lowest
275 cost is saved in its associated grid cell. A “mask” identifying grid cells where there are
276 known, persistent sources of NO_2 was developed for use in the algorithm; no V_{init} values
277 are stored in masked grid cells. The V_{init} values are averaged in the meridional direction
278 with a boxcar function of half width 5° . For each 1° latitude band, a wave analysis is
279 performed, fitting waves 0, 1, and 2, to give a preliminary background field. Grid cells
280 whose V_{init} value exceeds the preliminary background field by more than one standard
281 deviation are then excluded, and the wave analysis is redone. The result of this is a
282 background field (V_{bg}) that has been influenced very little by the presence of regions
283 of high NO_2 concentration. Since the V_{init} values were obtained using an AMF that is
284 appropriate to a profile having most of the NO_2 in the stratosphere, no further correction
285 to the background field is required.

3.4. Vertical column densities

286 For each FOV, the value of V_{init} is compared to the evaluated background field at that
287 location. If V_{init} is less than the background field, then the final value of V (the total NO_2
288 column amount) is taken to be V_{init} . If V_{init} is larger than the background field, then the
289 “polluted” part ($V_{\text{init}} - V_{\text{bg}}$) is scaled by the ratio $\text{AMF}_{\text{init}}/\text{AMF}_{\text{pol}}$, where AMF_{pol} is obtained
290 using the climatological GEOS-CHEM-modeled profile [*Bey et al.*, 2001; *Martin et al.*, 2002].
291 This procedure gives the total column, the background column, and the polluted column.
292 In addition, a tropospheric column, equal, in the polluted case, to the polluted column
293 plus the amount of the unpolluted profile that exists below the tropopause (assumed to

Federal Space Pole, Belgian Institute for

294 be at 200 hPa). Finally, if, according to the standard cloud product, the cloud fraction is
295 larger than 0.1, then the “below cloud amount” (the amount of NO₂ that is inferred to
296 be below the visible surface of the clouds) is also computed.

3.5. Destriping

297 Due to radiometric calibration and dark-current drift in OMI’s CCD detectors, which
298 affects the radiance measurements differently from the irradiance measurements, nearly
299 all OMI Level-2 data products show some degree of cross-track bias, which appears as
300 stripes of systematically elevated or diminished values at certain cross-track scan positions,
301 persisting throughout each orbital track [*Dobber et al.*, 2006]. While the origin of much
302 of the cross-track bias is now understood, and an improvement in the Level-0 to Level-1
303 processing algorithm is being implemented, the data available for the purpose of validation
304 to date have had significant cross-track bias.

305 A “destriping” procedure has been implemented in the OMI NO₂ algorithm. In this
306 procedure, the NO₂ SCDs and AMFs are collected for the 15 orbits (or fewer, depending on
307 data availability) used to construct the background field. These are then used to construct
308 separate SCD correction offsets for the northern and southern hemispheres:

$$\Delta_i = \overline{\text{SCD}_i} - \overline{\text{AMF}_i} \cdot \frac{\langle \text{SCD} \rangle}{\langle \text{AMF} \rangle}, \quad (4)$$

Space Aeronomy, 3 Avenue Circulaire,

B-1180 Brussels, Belgium

⁸Laboratory for Atmospheric Research,
Dept. of Civil and Environmental
Engineering, Washington State University,
Pullman, WA 99164-2910, USA

⁹Science Division, NASA Jet Propulsion
Laboratory, California Institute of
Technology, Pasadena, CA 91109

¹⁰Netherlands National Institute for
Public Health and the Environment
(RIVM), Bilthoven, The Netherlands

¹¹Institute for Environmental Physics,
University of Bremen, D-28334 Bremen,
Germany

¹²Max-Planck-Institute for Chemistry,
Mainz, Germany

¹³Institute for Environmental Physics,
University of Heidelberg, D-69120
Heidelberg, Germany

309 where i is the cross-track scan position (1 to 60), the overlines indicate averages for single
310 scan positions, and angle-brackets indicate averages over all scan positions. The Δ_i are
311 subtracted from the SCDS before applying the final air mass factors.

312 One concern about this procedure has been that it could introduce an unknowable bias
313 in the computed NO₂ column densities. This will be discussed in light of the ground-based
314 validation data.

4. Validation of OMI NO₂ columns

4.1. Stratospheric column

315 4.1.1. SAOZ and DOAS instruments in the NDACC network

316 The NDACC (Network for the Detection of Atmospheric Composition Change) is an
317 international cooperative network that coordinates the operations and data analysis at
318 more than 30 stations at various latitudes on the globe from 76°S to 79°N. The ground-
319 based UV-Visible zenith-sky spectrometers include both SAOZ (*Système d'Analyse par*
320 *Observations Zénithales*) as well as DOAS instruments, which provide ozone and NO₂ ver-
321 tical columns at sunrise and sunset using the Differential Optical Absorption Spectroscopy
322 (DOAS) technique [Platt, 1994] in the spectral range 410–530 nm. Zenith-sky measure-
323 ments made at solar zenith angles between 86–91° are averaged to give estimates of the
324 column NO₂. Because of the optical geometry of the measurement, the retrieved NO₂
325 column is much more sensitive to the stratospheric NO₂ column than to the tropospheric
326 column. Most of the instruments are located in remote geographical regions, far from
327 any significant source of tropospheric NO₂. Figure 2 shows the geographical distribution
328 of the SAOZ stations. Only the instruments at the Observatoire Haute-Provence (OHP),
329 France, and Bauru, Brazil, are in any proximity to presumed anthropogenic sources of

330 NO₂. Measurements from the SAOZ instruments have been previously used to compare
331 with NO₂ measurements by the space borne GOME and SCIAMACHY instruments [*Ionov*
332 *et al.*, 2006a, b, 2007; *Piters et al.*, 2006; *Lambert et al.*, 2001].

333 Stratospheric NO₂ exhibits a pronounced diurnal cycle due to its daytime photolysis
334 into NO and nighttime conversion into N₂O₅, as described in Section 1.1. The NO₂ daily
335 cycle starts with a fast drop shortly after sunrise, followed by a quasi-linear slow increase
336 during the day, a fast increase at sunset, and finally a slow decrease during the night.
337 The diurnal cycle has been simulated with a photochemical box model derived from the
338 SLIMCAT 3D chemical-transport model [*Denis*, 2005]. It includes 98 chemical and 39
339 photochemical reactions, including heterogeneous chemistry on liquid and solid particles.
340 Calculations are made at 17 altitude levels with a time step of 1 minute. The NO₂ total
341 column is obtained by integrating the profile assuming a constant density in each layer.
342 Figure 3 shows the results of simulations at two SAOZ stations, OHP at mid-latitude and
343 and Scoresby Sund in the Arctic, for summer and winter. Using this photochemical model,
344 a diurnal time series of the ratio NO₂(sunrise)/NO₂(*t*) was calculated for each month, and
345 at each SAOZ location. As SAOZ is an average of measurements between 86° and 91° SZA
346 the NO₂ column at 88.5° SZA is taken as the sunrise reference. All OMI measurements
347 were normalized to corresponding sunrise values using these ratios.

348 The optical geometry of the twilight SAOZ measurements is such that the light paths
349 traverse rather large distances through the stratosphere, so the stratosphere is sampled at
350 some distance from the measurement site. This should be taken into account when seeking

351 “match up” satellite FOVs corresponding to the ground-based measurements, especially
352 in regions with large stratospheric NO₂ gradients.

353 Finally, the OMI NO₂ algorithm provides total column NO₂, and the tropospheric col-
354 umn NO₂. Since SAOZ measurements are roughly 50 times as sensitive to the stratospheric
355 column as to the tropospheric column, it is of interest to compare the SAOZ-derived values
356 to the difference of the total and the tropospheric columns.

357 Figure 4 shows the time series of the difference between the sunrise SAOZ measurements
358 and the matching OMI measurements from eight SAOZ sites, adjusted to account for the
359 difference between the satellite overpass time and sunrise. The statistical characteristics of
360 these differences are presented in Table 1. Besides a comparison to just the stratospheric
361 column, the table presents a comparison between the OMI total column and the SAOZ
362 instrument measurements. It is seen that, at virtually all latitudes, there is very good
363 agreement, on average, between the ground-based and satellite-based measurements of
364 the total stratospheric NO₂ column. However, a small annual cycle is apparent in the
365 time-series for the higher latitudes, with lower values in the winter than in the summer.
366 This cycle, which appears in both the northern and southern hemisphere high latitudes,
367 may be related to the OMI sampling under those conditions, or may reflect a sensitivity
368 to the choice of matching OMI FOV corresponding to a given ground-based observation,
369 or may be due to a bias either in the satellite measurement at high solar zenith angle,
370 or in the ground-based measurements as the sunrise azimuth tends poleward. While the

371 influence of the seasonal cycle on the overall statistics is fairly small, understanding it
372 may be an avenue of further study.

373 The correlation coefficients between the SAOZ and OMI-measured stratospheric NO₂
374 columns are better, and the mean absolute differences smaller, for the mid-to-high latitude
375 sites than for the tropical sites. Since the stratospheric NO₂ concentrations are smaller
376 in the tropics in the first place (annual mean of about $2.5 \times 10^{15} \text{ cm}^{-2}$, compared to an
377 annual mean of $4 - 5 \times 10^{15} \text{ cm}^{-2}$ at the high latitude sites), the *relative* differences are
378 much greater in the tropics, and even the mid-latitude sites (OHP and Kerguelen), than
379 at the high-latitude sites.

4.2. Tropospheric column

380 4.2.1. MAX-DOAS

381 The MultiAxis DOAS (MAX-DOAS) technique is an extension of the zenith-sky DOAS
382 technique described in Section 4.1.1, but having much greater sensitivity to lower tro-
383 pospheric layers. In brief, a MAX-DOAS typically consists of two main parts: A grating
384 spectrometer mounted inside a thermostatted box that is located inside a building, and
385 one or more scanning telescopes connected to the spectrometer via fiber optics. Consec-
386 utive measurements at increasing elevation angles are performed in an acquisition cycle
387 that always contains observations at a number of low elevations, and a zenith observation.

388 From each of the measurements, a slant column is retrieved using the DOAS method
389 described in Section 4.1.1[*Platt, 1994*]. Besides NO₂, a number of other absorbers, plus
390 the Ring effect, are included in the fit, as are a multiplicative polynomial and an additive
391 polynomial for stray light correction. In order to account for the temperature depen-
392 dence of the NO₂ absorption spectrum, a second cross-section (295 K and 221 K) may

393 be introduced in the retrieval to improve the fit and correct the derived vertical column.
394 This potentially allows one to derive the effective air temperature at the centroid of the
395 NO₂ profile. It should be noted that not all retrievals used NO₂ cross-sections at two
396 temperatures, so systematic differences between different data sets may exist.

397 The lowest-elevation measurements have a large sensitivity to absorption in the bound-
398 ary layer, while the zenith measurements are used as background reference spectra which
399 contain Fraunhofer structures and the stratospheric absorption features. Since photon
400 scattering largely occurs below the tropopause, the photons collected from different el-
401 evation angles have essentially the same stratospheric path, but different light paths in
402 the troposphere. The difference between successive off-axis line-of-sight (LOS) and zenith
403 measurements is therefore only sensitive to the troposphere. For NO₂ retrieval, radiative
404 transfer simulations show that under polluted conditions, the stratospheric contamination
405 is generally smaller than 1%. A more in-depth description of the MAX-DOAS measure-
406 ments, as they were done at the DANDELIONS campaign, can be found in *Brinksmas et al.*
407 [2007].

408 An application that is under development, is the retrieval of boundary layer profile
409 information [*Wittrock, 2006*]. This is done by applying an optimal estimation method to
410 the observations from different elevation angles, yielding profile information for roughly
411 the first 2.5 km, with about 5 independent pieces of information. Experimental NO₂
412 profiles were retrieved from the 2005 Bremen MAX-DOAS data, but are not yet ready for
413 publication (F. Wittrock, private communication).

414 During the DANDELIONS campaigns [*Brinksmas et al., 2007*], various MAX-DOAS instru-
415 ments operated quasi continuously from the Cabauw Experimental Site for Atmospheric

416 Research [*Russchenberg et al.*, 2005] throughout May through mid July 2005 and through-
417 out September 2006. These instruments were provided and operated by BIRA-IASB, the
418 University of Bremen, and the University of Heidelberg.

419 The Heidelberg MAX-DOAS instrument differs from the others in that it has a set of
420 three movable telescopes, which enable simultaneous measurement cycles in three azimuth
421 viewing directions. The individual quartz fibers from each bundle associated with the
422 three different telescopes are arranged in a vertical column at the entrance slit of the
423 spectrograph (with two gaps between the three fiber bundles, see *Wagner et al.* [2004]).

424 For the Bremen instrument [*Wittrock et al.*, 2004], the zenith direction is viewed without
425 a mirror, while the other elevation angles in the measurement cycle are selected through a
426 rotating mirror inside the telescope. The range of elevation angles is $0^\circ - 30^\circ$. In the 2006
427 DANDELIONS campaign, separate UV and VIS instruments were operated by the Bremen
428 group.

429 **4.2.2. Agreement Between MAXDOAS Instruments**

430 The level of agreement achieved between the MAX-DOAS instruments is quantitatively
431 summarized in correlation plots (Fig. 5) where tropospheric NO_2 columns from the BIRA
432 instrument are compared to those from the other groups, for the 2005 campaign. Very
433 good agreement is found between the BIRA and Bremen data sets (Pearson correlation
434 coefficients of 0.9 and slope of 1.1), and also between BIRA and the three Heidelberg
435 telescopes (correlations between 0.82 and 0.91), especially considering that the BIRA
436 instrument was 200 m away from the other two instruments.

437 When the BIRA and Heidelberg data sets were re-retrieved using identical NO_2 absorp-
438 tion cross-sections, an even better agreement is found, reaching a correlation coefficient

439 of 0.92 and a slope of 0.99. This level of agreement is only achieved when considering the
440 southwest-pointing Heidelberg telescope: this is approximately in the same direction as
441 the two other instruments. This highlights the importance of horizontal inhomogeneities
442 in the NO₂ field that in some cases strongly affect the agreement between ground based
443 and satellite based measurements.

444 **4.2.3. Heterogeneity of the NO₂ Field**

445 Assuming that the tropospheric NO₂ layer is horizontally homogenous, the observed
446 NO₂ SCDs for the different azimuth angles observed from the three telescopes of the Hei-
447 delberg instrument should have been similar. In turn, from the observed differences for the
448 various viewing directions, the horizontal heterogeneity of the NO₂ concentration field can
449 be estimated. Such an estimation is very important for the validation of satellite instru-
450 ments with ground based observations. In cases of strong horizontal gradients, ground
451 based observations may not be representative for the average value within a satellite
452 ground pixel.

453 Since the horizontal extension of the absorption paths along the line of sight is largest
454 for low telescope elevation, we used those at 3° to estimate the heterogeneity of the
455 tropospheric NO₂ concentration field. We did this by evaluating the SCD in the three
456 azimuthal viewing directions at 3° elevation, and calculating the ratio of the maximum
457 and the minimum. A horizontally homogenous concentration field yields a ratio of one; the
458 more this ratio deviates from unity, the larger are the horizontal gradients. In addition to
459 the strength of the horizontal gradients, the direction of the NO₂ gradient was estimated,
460 though in a limited way, since the Heidelberg MAX-DOAS was measuring in only three
461 azimuth directions. Fig. 6 displays the time series of the ratios at daily noon. High ratios

462 indicate strong gradients, and the color of the points indicates the direction of positive
463 gradient.

464 For the interpretation of the retrieved information on the gradient of the tropospheric
465 NO₂ concentration field, it is important to consider two effects that can affect the observed
466 SCDs, especially for low elevation angles: First, the sensitivity to the relative azimuth
467 angle (between the telescope and the sun). This dependency becomes more pronounced
468 for increasing solar zenith angle (SZA) and increasing aerosol load [*Wagner et al.*, 2004].
469 Second, the effect of the atmospheric aerosol load on the atmospheric visibility, and thus
470 on the horizontal extents of the absorption paths along the line of sight. Thus, depending
471 on the aerosol load, the calculated ratio represents information on gradients over areas
472 of different horizontal extent. The dependence on the azimuth angle was found to be
473 below 15%, for SZA between 20° and 80°. Almost all observed ratios of the maximum and
474 minimum NO₂ SCDs (see Fig. 6) were much larger than this. Effective path lengths are
475 enhanced by aerosols above about 1 km, and diminished by aerosols below 1 km. For an
476 elevation angle of 3°, the effective path length is about 19 km in a pure Rayleigh-scattering
477 atmosphere, but this can be reduced to as little as 4.5 km by surface-level aerosols, or
478 enhanced to 25 km by higher-altitude aerosols [*Brinkma et al.*, 2007; *Deutschmann and*
479 *Wagner*, 2006; *Wagner et al.*, 2007, 2004].

480 **4.2.4. Comparisons with OMI tropospheric NO₂**

481 The different MAX-DOAS data sets have been compared to the OMI level 2 and level 4
482 cloud-free data (O₂–O₂ cloud fractions in the OMI products less than 20%) for 2005. In
483 order to produce the correlation plots presented in Fig. 7, the MAX-DOAS data have been

484 linearly interpolated to the satellite overpass time. The corresponding regression analysis
485 parameters are given in Table 2.

486 For the two OMI algorithms, the vertical columns were generally distributed in values
487 ranging from 0 to about 2.5×10^{16} molec cm⁻². In one case the ground based MAX-DOAS
488 column (3×10^{16} molec cm⁻²) significantly exceeded the corresponding satellite values,
489 possibly due to a local enhancement of the NO₂ concentration at Cabauw. A second outlier
490 (reported between parentheses in the Figure) was noted in the OMI Level 4 products. In
491 this outlier case, the reported NO₂ column was twice as large as the corresponding value
492 in the OMI Level 2 product. Because of its obvious anomaly, this point has been excluded
493 from the regression analysis. The strong overestimation of the tropospheric NO₂ column
494 obtained in this case with the OMI Level 4 product points to a possible algorithm problem,
495 which might eventually be related to the model profile shape used for the AMF calculation
496 and the calculation of the ghost column for the cloudy part of the pixel. More work is
497 needed to better understand the origin of the problem.

498 The regression analyses show that similar results were achieved with the BIRA and the
499 Bremen data sets, the correlation coefficient between ground based and satellite data being
500 about 0.6 for OMI level 2 and about 0.5 for OMI level 4. A lower correlation was obtained
501 with the Heidelberg data when considering only the southwest direction measurements
502 (closest to the viewing direction of both Bremen and BIRA instruments), possibly due to
503 the smaller number of coincidences with this instrument, and also the shorter integration
504 time used, which may increase the sensitivity to local inhomogeneities in the NO₂ field.
505 In order to further explore the impact of possible horizontal smoothing effects on the
506 comparison results, the Heidelberg measurements simultaneously recorded from all three

507 directions have been averaged and again compared with satellite data. The resulting
508 correlation coefficients, also given in Table 2, have significantly improved and are now
509 the highest of the three MAX-DOAS instruments. This suggests that the scatter in MAX-
510 DOAS versus satellite comparisons is, indeed, largely dominated by spatial (and temporal)
511 averaging effects.

512 As is evident from the regression results, the OMI tropospheric NO₂ columns seem to be
513 systematically lower than the MAX-DOAS results, for both OMI products considered. How-
514 ever, it must be noted that the correlation coefficients are rather poor in all cases, which
515 might be due to several reasons including uncertainties in both ground based (geometrical
516 approximation) and satellite retrievals (AMF sensitivity to errors in aerosols, clouds and
517 NO₂ profile shape). As already mentioned, the main reason for the poor correlation is
518 probably related to the spatial mismatch between the ground based MAX-DOAS observa-
519 tion (essentially local) and the satellite measurements (averaged over the OMI footprint).
520 One expects that the collection of more comparison points will help in improving the sta-
521 tistical significance of the comparisons. Hence further studies will be conducted bringing
522 in measurement data from the second DANDELIONS campaign. This and detailed valida-
523 tion of the satellite retrievals during the campaigns is the topic of another publication
524 (G. Pinardi et al., in preparation). That paper will look into different algorithm results,
525 strength of collocation criteria, role of ghost columns, and, for OMI, also dependence on
526 FOV cross-track angle.

4.3. Total column

527 4.3.1. Brewer

528 *Cede et al.* [2006] have described a method for retrieval of total-column NO₂ from direct-
529 sun measurements using a Brewer MK-III double monochromator spectrophotometer. The
530 Brewer MK-III instrument was primarily designed to make measurements of ozone from
531 wavelengths below 320 nm, and can measure spectral irradiance and radiance from 285
532 to 365 nm. Its measurement modes include a spectral scan mode, where the gratings
533 are moved and any wavelength can be selected, and a slit mask mode, in which a slit
534 mask is introduced in the optical path allowing nearly simultaneous measurements at 6
535 wavelengths, spaced about 3 nm apart. The spacing of the slits in the slit mask was
536 chosen to optimize the ozone retrievals between 303 and 320 nm, but in the 345–365 nm
537 range the measured wavelengths fall very nearly on maxima and minima in the NO₂
538 absorption spectrum (see Figure 8), which permits the retrieval of total column NO₂.
539 These measurements have been made at the NASA Goddard Space Flight Center, on a
540 nearly continual basis since August 2004, with measurements made every half hour during
541 the sunlit hours.

542 The retrieved NO₂ columns have a large instrumental noise, so data must be averaged
543 over several hours time in order to make meaningful comparisons to the OMI-measured
544 values. However, the location of the instrument, which is situated 3 km from the Washing-
545 ton Capital Beltway and 2 km from the Baltimore-Washington Parkway, on the outskirts
546 of a major metropolitan area, is such that there are often substantial sub-hour time vari-
547 ations in the actual tropospheric NO₂ concentrations. The combination of the intrinsic
548 variability of the measurements with the frequent occurrence of significant actual concen-
549 tration variations within a given time-window used for collocation with OMI overpasses
550 complicates the process of using the Brewer data for validation of OMI NO₂ measurements.

551 Comparisons having useful statistical significance can be made using monthly averages of
552 the Brewer and OMI datasets.

553 Figure 9 shows the comparison between the monthly mean Brewer-measured and OMI-
554 measured NO_2 columns. In the Washington DC area, early afternoon NO_2 columns are
555 dominated by the boundary layer columns. The difference that is seen, with OMI-measured
556 columns that are about 35% smaller than the Brewer-measured columns, can thus be
557 largely attributed to the tropospheric NO_2 . In Figure 10 the daily and monthly mean
558 values are plotted, along with the line of linear regression to the monthly means. The
559 regression analysis, performed on the monthly means, and weighted according to the
560 standard deviations, gives a slope of 0.67, with a correlation coefficient $R = 0.95$.

561 **4.3.2. MultiFunction DOAS (MFDOAS) measurements**

562 The MF-DOAS instrument observes scattered skylight with a 1° vertical FOV at varying
563 viewing azimuth and elevation angles, as well as direct sunlight in the UV-visible spectral
564 region. From these measurements are retrieved NO_2 , O_3 , SO_2 , and CH_2O slant columns.
565 The MF-DOAS spectrograph is a single pass commercial Czerny-Turner spectrograph of
566 focal length 300 mm. The instrument covers a wavelength range from 280 nm to 490 nm
567 with a spectral resolution of 0.82 nm (6 pixels FWHM). Scattered sky light is collected by
568 a 12 cm telescope and passes into the spectrograph through two filter wheels that contain
569 depolarizers, spectral flattening filters, and UV cutoff filters. Direct sunlight is fed into
570 a spectralon integrating sphere of diameter 8 cm before passing through the filter wheels
571 and results in a signal level similar to that from the scattered sky. A two-dimensional
572 CCD detector (512×2048 pixels) is used in the focal plane. Spectrograph stray light is
573 reduced by a spectral flattening filter, which reduces the long wavelength throughput of

574 the instrument relative to the short wavelength signal. A solar tracker moves the entire
575 instrument for positioning and sun tracking. An instrument schematic is presented in
576 Figure 11.

577 This ground-based MF-DOAS instrument was fielded in a prototype form during the
578 INTEX-B campaign for Aura/OMI validation. It was positioned on the roof of a building at
579 Pacific Northwest National Laboratory in Richland, WA (PNNL; 46.3409°N, 119.2787°W),
580 located in an urban area known as Tri-Cities (the merged cities of Kennewick, Pasco and
581 Richland, WA) with total population of approximately 150,000 in an area of 250 km².
582 PNNL is situated approximately 15 km north of the center of Richland, and northwest
583 of the area's population center. The major source of local NO₂ pollution is vehicular
584 exhaust.

585 NO₂ differential slant columns (DSCD) were derived using the DOAS technique, based
586 on Beers law. A nonlinear least squares algorithm was used to fit our measured spectral
587 cross sections of NO₂, O₃, instrument spectral polarization, and Ring effect in the spectral
588 region 400–419 nm. A polynomial was included to remove slowly varying Rayleigh and
589 Mie scattering spectral shapes. The reference solar spectrum used for the data analysis
590 was measured at zenith at local noon on April 30, 2006, a day with very low pollution
591 levels. Raw spectra were corrected for detector dark background and flat field. Figure
592 12 shows typical residual optical densities after the least squares fitting procedure for
593 observations taken on May 9, 2006 at 5° elevation and 4 azimuth angles. The LIDORT
594 radiative transfer code [*Spurr*, 2001; *Spurr et al.*, 2001] was used to calculate the air mass
595 factors (AMF) to convert the DSCD to vertical column density (VCD). As an example of
596 the results, Figure 13 presents the spatial and temporal variation of NO₂ differential slant

597 column for May 9, a polluted day. Higher column densities were observed to the south and
598 east, toward the urban center, as expected. Measurements taken at 5° elevation showed
599 higher NO₂ tropospheric column compared to 15° and 45° angles, as expected. These
600 elevated NO₂ slant column densities were particularly pronounced during the morning
601 rush hour.

602 The Aura satellite flies over Tri-Cities area around 1330h with spatial resolution ap-
603 proximately 13 km × 24 km. Figure 14 shows contour plots of OMI tropospheric NO₂ VCD
604 for May 9, derived from the Level-2 OMI data product. OMI tropospheric NO₂ vertical
605 column densities “integrated” over several pixels in the MF-DOAS observation direction
606 were compared to MF-DOAS tropospheric NO₂ VCD using *a priori* differential AMFs for
607 clear days at PNNL from the LIDORT radiative transfer code. Figure 15 shows results for
608 the time period April 30 through May 13, 2006, with reasonable correlation observed for
609 these clear days.

610 The slope of the data in Figure 15 shows that OMI determinations of tropospheric NO₂
611 VCD are 0.81 ± 0.11 of that determined from MF-DOAS with a correlation coefficient R^2 of
612 0.92. Thus, OMI measures a somewhat smaller VCD than that determined from MF-DOAS.

613 **4.3.3. Pandora-1 Direct Sun DOAS measurements**

614 The lightweight, portable Pandora-1 spectrometer system measures direct-sun irradi-
615 ances from 270 to 500 nm at ~ 0.5 nm resolution. The outdoor head sensor is mounted
616 on a tracking system and holds a single strand fiber optic cable, which collects the light
617 passed through a collimator (1.6° FWHM field of view) and a filter wheel. The other
618 end of the fiber is connected to a 75 mm focal length symmetric Czerny-Turner grating
619 spectrometer using a 1024 × 1 pixel CMOS detector, stabilized to $20^\circ \pm 1$. The total NO₂

620 column is retrieved by the DOAS method, in the 400–440 nm window, using a fixed ref-
621 erence spectrum determined from Pandora-1 data obtained over an extended period of
622 at least 2 weeks. To estimate the NO₂ amount in the reference spectrum, a bootstrap
623 method as described in *Cede et al.* [2006] was applied, on the assumption that a few
624 measurements were obtained when there were low tropospheric NO₂ amounts (e.g., just
625 after sunrise). Figure 16 shows Pandora-1 data during the SCOUT campaign in July 2006
626 at Thessaloniki, Greece. Excellent agreement is seen between the OMI and Pandora-1
627 measurements, though the OMI overpass times seem to occur just before or just after the
628 mid-day maximum in NO₂ concentration; this limits the range of NO₂ concentration val-
629 ues explored in this comparison. A number of further field campaigns are planned, during
630 which Pandora-1/OMI comparisons will be done.

631 4.3.4. Direct Sun DOAS (BIRA)

632 During the second DANDELIONS campaign, a direct-sun DOAS instrument was operated
633 in addition to the MAX-DOAS instrument. The well-defined optical path and air mass
634 factor make this instrument equally sensitive to absorption along the whole optical path
635 and so provides accurate NO₂ total columns.

636 The instrument is similar in concept to the MAX-DOAS: Inside the building, in a thermo-
637 regulated box, a grating spectrometer covering the UV-Vis region is coupled to a cooled
638 CCD detector, connected by depolarizing fiber optic bundle to the external optical head.
639 Outside, alongside the MAX-DOAS scanning telescope, a collimating optic tube is mounted
640 on a BRUSAG commercial sun-tracking system, holding the fiber.

641 The retrieval is also done using the DOAS approach: The ratios of the measured radiance
642 spectra to a reference spectrum are analyzed with respect to a set of reference spectra,

643 in the 425–450 nm window, including laboratory spectra of O₃, H₂O, O₂–O₂, the com-
644 puted the Ring effect spectrum, and NO₂ cross-sections at two different temperatures. In
645 contrast to the analysis of MAX-DOAS data, a fixed reference spectrum (measured on 7
646 September 2006) has been used for the whole time-series. The NO₂ residual slant column
647 amount included in this reference spectrum has been obtained by analysing it with re-
648 spect to the Kurucz solar atlas [*Kurucz et al.*, 1984], which was assumed to be free of NO₂
649 absorption. The Kurucz solar spectrum was convolved with a precisely measured instru-
650 ment slit function to match the instrument’s spectral resolution. Based on this analysis,
651 total absolute slant columns could be derived from direct sun measurements; these were
652 transformed into total vertical columns using geometrical AMFs.

653 Figure 17 shows the time series for the BIRA DOAS measurements of the total column
654 NO₂ (filled dots), which provides a good idea of the diurnal variation of NO₂ levels.
655 The open squares show the collocated OMI measurements (one or two per day). The
656 OMI snapshots of vertical column NO₂, for the most part, appear to be in quite good
657 agreement with the ground-based measurements. Note that the OMI data are filtered for
658 clouds (cloud fraction $\leq 20\%$).

659 Figure 18 shows the correlation plot of the collocated data (the point nearest in time
660 to the OMI overpass). A linear regression, constrained to pass through the origin, gives a
661 slope of 0.84 ± 0.05 . The scatter in the data ($R = 0.68$), and the relatively small number
662 of data points ($N = 26$) do not permit a statistically significant estimation of an additive
663 bias.

664 4.3.5. FTUVS measurements at Table Mountain, California

665 Another instrument that has been used to validate OMI NO₂ total column measurements
666 uses the Fourier Transform Ultraviolet Visible Spectrometer (FTUVS), a UV-VIS-NIR in-
667 terferometer, at the Table Mountain Facility (TMF), north of Los Angeles, California, at
668 34°22.9' N, 117°40.8' W, at an altitude of 2290 m (7300') [Cageao *et al.*, 2001]. Spectra are
669 recorded in the direct solar absorption mode with a spectral resolution of 0.0013 nm, which
670 is sufficient to resolve NO₂ vibronic features. By measuring the doppler-shifted spectra
671 from the east and west solar limbs, and taking the ratio of the two, one can remove the
672 solar Fraunhofer lines; there is no need to measure a high-sun reference spectrum, as in a
673 number of the other methods described in this overview.

674 The instrument is not readily transportable. The FTUVS observation site overlooks the
675 Antelope Valley, north of the Los Angeles Basin. This area is characterized by relatively
676 clean air under most conditions, but is often influenced by polluted air from Los Angeles
677 in the afternoon, advected through the Cajon Pass. While considerably above the tro-
678 pospheric background under these conditions, the NO₂ column abundance values rarely
679 exceed 1×10^{16} molecules cm⁻², which is considerably smaller than values measured di-
680 rectly downwind of a polluted urban area (see Fig. 9). Because the altitude of TMF is
681 about 2500 feet above the Antelope Valley, FTUVS column abundance measurements of
682 NO₂ will be biased relative to the center of the OMI footprint. The bias is small relative
683 to the total column, and will not have a significant effect on the slope of the OMI-FTUVS
684 correlation. The OMI data used for validation were sorted by distance from the TMF
685 site, in order to mitigate somewhat the possible effects of the distribution of elevations

686 within a FOV. It was found that a minimum distance of about 10 km is required for good
687 intercomparison.

688 The FTUVS instrument time is shared with other Aura validation activities. On average,
689 measurements were acquired twice a week over the period March–November, 2006.

690 The slant column NO₂ amounts are retrieved by fitting the measured absorption spectra
691 to laboratory spectra at a number of temperatures [*Nizkorodov et al.*, 2004], in windows
692 containing 10 to 20 NO₂ rotational lines. Geometric AMFs were used to convert the
693 SCDS to VCDs. Figure 19 presents the comparison of the OMI-derived and FTUVS-derived
694 measurements of total column NO₂. In this figure, the points where the OMI FOV center
695 fell within 10 km of the Table Mountain Facility site are colored red. The linear regression
696 line shown is fit only to those points. As shown, this line has a slope of 0.77 ± 0.41 , and
697 it does not go through the origin. This data set suggests that the OMI NO₂ totals are
698 underestimated in the middle of the data range, but that there may also be a positive
699 additive bias.

4.4. NO₂ Profile measurements

700 As pointed out in previous sections, and in *Boersma et al.* [2002] and *Bucsela et al.*
701 [2006], the shape of the vertical profile of NO₂ influences the (physical) air mass fac-
702 tors. The OMI NO₂ algorithm uses a set of assumed profiles, which were derived from
703 model studies; these assumed profiles thus affect the retrieved total and tropospheric NO₂
704 amounts. It is therefore important to evaluate how well the assumed profiles approximate
705 the actual profiles, *vis-à-vis* the air mass factor calculation. There have been very few
706 efforts to measure NO₂ profiles [*Heland et al.*, 2002; *Martin et al.*, 2006]. Recent efforts
707 include measurements during the September 2006 DANDELIONS campaign (lidar, *in situ*

708 at two altitudes, and MAX-DOAS at two altitudes, see section 4.4.1), and aircraft-based *in*
709 *situ* measurements taken during the INTEX-B campaign in North America.

710 4.4.1. NO₂ lidar

711 NO₂ profiles were measured by a lidar system, developed at RIVM, during the DAN-
712 DELIONS campaign in September 2006 [Brinkma *et al.*, 2007]. The lidar consists of an
713 emitter and a receiver unit. The entire system is housed in a truck, constituting a fully
714 self-supporting mobile laboratory. The emitter unit consists of a pulsed pump laser-dye
715 laser combination, running at 30 Hz. The dye laser is tuned to 449.10 nm and detuned
716 to 448.31 nm every other pulse. The latter wavelength is absorbed more strongly by NO₂
717 than the former. The laser pulses, 40 mJ in energy, 10 ns in duration, are directed into the
718 atmosphere, where they are scattered by gas molecules and aerosol particles. The receiver
719 unit collects the backscattered light, through a 280 mm telescope, onto a photomultiplier
720 tube, with an interference filter to block daylight. A digitizer samples the signals with a
721 range resolution of 3.75 m.

722 The NO₂ concentration at a certain altitude is derived from the log of the ratio of
723 the backscattered signals at the two wavelengths, using the differential absorption lidar
724 (DIAL) method. Since the laser pulses are not emitted from the center of the telescope, the
725 laser beam is not in view of the telescope at close range, and thus the lidar is effectively
726 blind for the first 500 m. When measurements starting near the surface are required, the
727 emitter section and receiving telescope are tilted through various elevation angles; the
728 measurements are combined into a single profile, where elevations close to the horizontal
729 yield NO₂ concentrations at low altitudes but pertaining to a certain horizontal extent
730 away from the instrument (for a near-horizontal measurement, typically about 2500 m),

731 while a zenith observation is performed exactly above the truck. Completing one vertical
732 profile typically takes 50 minutes, providing data in a altitude range of a few meters up to
733 approximately 2500 m, with an accuracy of 0.2–0.4 $\mu\text{g m}^{-3}$. Range and accuracy depend
734 on atmospheric conditions. The vertical resolution of a profile varies, and typically is
735 about 15 m at the lowest altitude, increasing to over 500 m at the highest altitude. The
736 resolution arises from averaging of data over an altitude range, based on signal-to-noise
737 considerations.

738 A paper describing the lidar and other time-resolved three dimensional observations
739 of NO_2 during the 2006 DANDELIONS campaign is in preparation (H. Volten et al., in
740 preparation).

741 Figure 20 presents examples of profile measurements for a relatively clean day, Septem-
742 ber 9, 2006, and for a polluted day, September 12, 2006; in both cases, there was little-
743 to-no cloud cover. The concentration of NO_2 is high at ground level, and drops to zero
744 (within the accuracy of the measurement) above the boundary layer. The boundary layer
745 heights, provided by the boundary layer lidar at Cabauw, are indicated in Figure 20 by a
746 dashed line. The figure shows that the day-to-day variations in NO_2 at the surface may
747 be considerable, from around 3 $\mu\text{g NO}_2 \text{ m}^{-3}$ on a clean day to more than 50 $\mu\text{g NO}_2 \text{ m}^{-3}$
748 on a polluted day. Large diurnal variations may also occur.

749 4.4.2. In-situ aircraft measurements

750 *In situ* measurements of NO_2 from the DC-8 aircraft were obtained during the INTEX-A
751 (summer 2004), PAVE (winter 2005) and INTEX-B (spring 2006) campaigns. These have
752 been discussed by *Bucsela et al.* [2007]. The NO_2 profiles from these experiments are useful
753 for validating both the shapes of the model profiles used in the OMI retrieval algorithm,

754 and, in turn, the tropospheric column amounts from the satellite retrievals. The aircraft
755 profiles obtained during INTEX-A and PAVE were combined into composite land and ocean
756 profiles. The *in situ* profiles were seen to be very similar to the annual mean GEOS-CHEM
757 profiles used to retrieve tropospheric NO₂ columns from OMI, and the AMFs computed from
758 the measured profiles were slightly larger than those calculated using the model profiles.
759 A more quantitative analysis was performed using a set of approximately 70 profiles
760 measured during INTEX-B. Error-weighted linear regressions comparing the AMFs yielded
761 a slope of 1.10 ± 0.10 (*in situ* profile AMF greater than that used by the OMI algorithm).
762 This means that the OMI VCD would overestimate the actual VCD by 10%(±10%).

763 *In situ* measurements of NO₂ can also be used to validate tropospheric column amounts
764 from OMI. The INTEX-B data were used for this analysis by *Bucsela et al.* [2007] (see
765 also *Boersma et al.* [2007]). Two representative profile analyses are shown in Figure 21.
766 The full set of profiles from INTEX-B were used. The correlation between the aircraft
767 and OMI data sets was good ($R = 0.83$). This comparison is shown in Figure 22. The
768 integrated *in situ* tropospheric columns were found to be somewhat larger than the OMI
769 Level-2 columns, as indicated by the slope of 1.10 ± 0.08 . Although some of the *in situ*
770 columns required significant extrapolations, sensitivity studies indicated that the overall
771 results were generally robust with respect to the choices made for the profile binning,
772 integration and extrapolation, as well as being relatively insensitive to the errors assumed
773 for the weights. The insensitivity to extrapolation is consistent with findings in a similar
774 aircraft study by *Heland et al.* [2002].

5. Conclusions and discussion

775 This paper has presented a number of results of experiments where ground- and aircraft-
776 based measurements of NO₂ can be compared with collocated measurements and retrieval
777 by OMI. Since some measurements estimate the stratospheric column, others the tropo-
778 spheric column, and still others the total column, their results can be used to validate the
779 OMI NO₂ standard data product's estimates of these columns.

780 Table 3 summarizes the results of the numerous validation studies that have been dis-
781 cussed in this overview.

782 On the basis of the SAOZ and DOAS measurements, which are most sensitive to the
783 stratospheric NO₂ columns, the OMI stratospheric NO₂ appears to agree with the ground-
784 based measurements to within $\sim 10\%$.

785 The OMI tropospheric column appears to be consistently lower than the various ground-
786 based measurements, though there is some inconsistency amongst those ground-based
787 measurements. Though many of the various instruments and methods for measuring
788 tropospheric and total NO₂ have not themselves been validated, it is noteworthy that they
789 all give NO₂ estimates that are on average greater than those retrieved from OMI. This
790 may indicate a bias in the OMI retrieval. However, a number of cases have been studied,
791 where average differences between OMI and ground based measurements decrease as the
792 geographic match up criterion is tightened. It is likely to be due to the inhomogeneity of
793 the tropospheric NO₂ field, and, in particular, the fact that ground-based measurements
794 are often made in or near regions of moderate to strong sources of NO₂: The OMI FOV
795 that includes the site will also include a substantial ($\sim 10^2$ km²) regions where much lower
796 NO₂ concentrations prevail. This was borne out in the Brewer studies [*Cede et al.*, 2006]
797 and in the correlation studies of *Veeffkind et al.* [2007] (see also Section 1.) However, the

798 data taken at TMF (Section 4.3.5) were mostly obtained under conditions of relatively
799 clean tropospheric air, and these data also suggested a negative bias for OMI retrieval.

800 Potential biases can arise at any of the steps in the algorithm. Instrumental artifacts
801 are known to give rise to the cross-track bias (striping) and the destriping process can
802 certainly give rise to a general bias. The stratosphere-troposphere separation is based
803 on an initial AMF, and any bias in that AMF will result in a bias in the background
804 (mostly stratospheric) field. After the stratosphere-troposphere separation, a new AMF
805 is constructed, based on model-based-climatology derived *a priori* profiles. The aircraft
806 *in situ* measurements of NO₂ profile shape suggest that the *a priori* profile shapes are
807 essentially correct, in that the two do not give appreciably different AMFs. The AMF
808 is also sensitive to the surface albedo. The OMI algorithm uses a climatological surface
809 albedo, and this may be a worthy subject for future validation studies.

810 It should be mentioned that all the validation studies reviewed here focused on mostly
811 cloud-free conditions. However, while OMI FOVs are considerably smaller than those of

812 earlier atmospheric remote sensing instruments, they are still large enough that very few
813 can be expected to be completely uncontaminated by clouds.

814 Acknowledgments

815 Part of this research was carried out at the Jet Propulsion Laboratory, California Insti-
816 tute of Technology, under contract with the National Aeronautics and Space Administra-
817 tion.

References

References

- 818 Bey, I., D. J. Jacob, R. M. Yantosca, J. A. Logan, B. D. Field, A. M. Fiore, Q. Li, H. Y.
819 Liu, L. J. Mickley, and M. G. Schultz (2001), Global modeling of tropospheric chem-
820 istry with assimilated meteorology: Model description and evaluation, *J. Geophys.*
821 *Res.*, *106*, 23 073–23 096.
- 822 Boersma, K. F., E. Bucsela, E. Brinksma, and J. F. Gleason (2002), NO₂, in *OMI*
823 *Algorithm Theoretical Basis Document, Volume IV: Trace Gas Algorithms*, edited by
824 K. Chance, KNMI, NASA/GSFC, FMI, pp. 15–36.
- 825 Boersma, K. F., D. J. Jacob, E. J. Bucsela, A. E. Perring, R. Dirksen, R. J. van der A,
826 R. M. Yantosca, R. J. Park, and R. C. Cohen (2007), Validation of OMI tropospheric
827 NO₂ observations during INTEX-B and application to constrain NO_x emissions over
828 the eastern United States and Mexico, *J. Geophys. Res.*, —, doi:---, —.
- 829 Brinksma, E. J., G. Pinardi, R. Braak, H. Volten, A. Richter, A. Schönhardt, M. van
830 Roozendaal, C. Fayt, C. Hermans, R. J. Dirksen, T. Vlemmix, A. J. C. Berkhout,

831 D. P. J. Swart, H.Oetjen, F. Wittrock, T. Wagner, O. W. Ibrahim, G. de Leeuw,
832 M. Moerman, R. L. Curier, E. A. Celarier, W. H. Knap, J. P. Veefkind, H. J. Eskes,
833 M. Allaart, R. Rothe, A. J. M. Piters, and P. F. Levelt (2007), The 2005 and 2006
834 DANDELIONS NO₂ and aerosol validation campaigns, *J. Geophys. Res.*, —, —.

835 Bucselá, E., A. E. Perring, R. C. Cohen, J. F. Gleason, K. F. Boersma, M. O. Wenig,
836 T. H. Bertram, P. J. Wooldrige, R. Dirksen, E. A. Celarier, and J. Veefkind (2007),
837 A comparison of NO₂ *in situ* aircraft measurements with data from the Ozone Mon-
838 itoring Instrument, *J. Geophys. Res.*, —, doi:---, —.

839 Bucselá, E. J., E. A. Celarier, M. O. Wenig, J. F. Gleason, J. P. Veefkind, K. F.
840 Booersma, and E. J. Brinksma (2006), Algorithm for NO₂ vertical column retrieval
841 from the Ozone Monitoring Instrument, *IEEE Trans. Geosci. Rem. Sens.*, *44*(5),
842 doi:10.1109/TGRS.2005.863715, 1245–1258.

843 Burrows, J. P., A. Richter, A. Dehn, B. Deters, S. Himmelmann, S. Voigt, and J. Or-
844 phal (1999), Atmospheric remote sensing reference data from GOME-2. temperature-
845 dependent absorption cross-sections of O₃ in the 231-794 nm range, *J. Quant. Spec-*
846 *trosc. Radiat. Transfer*, *61*, 509517.

847 Cageao, R. P., J. F. Blavier, J. P. McGuire, Y. B. Jiang, V. Nemtchinov, F. P. Mills, and
848 S. P. Sander (2001), High resolution fourier transform ultraviolet-visible spectrometer
849 for the measurement of atmospheric trace species: Application to OH, *Appl. Opt.*, *40*,
850 2024–2030.

851 Cede, A., J. Herman, R. Richter, N. Krotkov, and J. Burrows (2006), Measurements of
852 nitrogen dioxide total column amounts using a brewer double spectrophotometer in
853 direct sun mode, *J. Geophys. Res.*, *111*, doi:10.1029/2005JD006585.

854 Celarier, E. A., J. F. Gleason, E. J. Bucsela, K. F. Boersma, E. Brinksma, J. P. Veefkind,
855 and P. Levelt (2006), OMNO2 README file, Tech. rep., NASA Goddard Space Flight
856 Center. URL http://toms.gsfc.nasa.gov/omi/no2/OMNO2_readme.pdf.

857 Chance, K. V. and R. J. D. Spurr (1997), Ring effect studies: Rayleigh scattering,
858 including molecular parameters for rotational Raman scattering, and the Fraunhofer
859 spectrum, *Appl. Opt.*, *36*(21), 5224–5230.

860 Cleary, P. A., P. J. Wooldridge, and R. C. Cohen (2002), Laser-induced fluorescence de-
861 tection of atmospheric NO₂ with a commercial diode laser and a supersonic expansion,
862 *Appl. Opt.*, *41*, 6950–6956.

863 Denis, L. e. a. (2005), A new software suite for NO₂ vertical profile retrieval from
864 ground-based zenith-sky spectrometers, *J. Quant. Spectrosc. Radiat. Transfer*, *92*(3),
865 321–333.

866 Deutschmann, T. and T. Wagner (2006), *TRACY-II Users manual*, University of Hei-
867 delberg.

868 Dobber, M., R. Dirksen, P. Levelt, G. van den Oord, R. Voors, Q. Kleipool, G. Jaross,
869 M. Kowalewski, E. Hilsenrath, G. Leppelmeier, J. de Vries, W. Dierssen, and N. Roze-
870 meijer (2006), Ozone monitoring instrument calibration, *IEEE Trans. Geosci. Rem.*
871 *Sens.*, *44*(5), doi:10.1109/TGRS.2006.869987, 1209–1238.

872 Gordley, L., J. Russell, L. Mickley, J. Frederick, J. Park, K. Stone, G. Beaver, J. McIn-
873 erness, L. Deaver, G. Toon, F. Murcray, R. Blatherwick, M. Gunson, J. Abbatt,
874 R. Mauldin, G. Mount, B. Sen, and J. Blavier (1996), Validation of nitric oxide
875 and nitrogen dioxide measurements made by the halogen occultation experiment for
876 UARS platform, *J. Geophys. Res.*, *101*(D6), doi:A1996UJ40400034, 10 241–10 266.

877 Heland, J., H. Schlager, A. Richter, and J. P. Burrows (2002), First comparison of
878 tropospheric NO₂ column densities retrieved from GOME measurements and in situ
879 aircraft profile measurements, *Geophys. Res. Lett.*, 29(20), Article No. 1983.

880 Ionov, D., F. Goutail, and J. Pommereau (2006a), Validation of satellite data on total
881 NO₂: GOME, SCIAMACHY and OMI nadir viewing instruments compared to UV-
882 visible SAOZ network, in *Proc. of 3rd International DOAS Workshop, Bremen, 20-22*
883 *March, 2006*, pp. —.

884 Ionov, D., F. Goutail, J.-P. Pommereau, A. Bazureau, E. Kyro, T. Portafaix, G. Held,
885 P. Ericksen, and V. Dorokhov (2006b), Ten years of NO₂ comparisons between ground-
886 based SAOZ and satellite instruments (GOME, SCIAMACHY, OMI), in *Atmospheric*
887 *Science Conference, ESRIN, Frascati, Italy, 8-12 May 2006*, ESA SP-628, pp. —.

888 Ionov, D., Y. Timofeyev, F. Goutail, J.-P. Pommereau, and A. Shalamyansky (2007),
889 Delta-validation of ENVISAT SCIAMACHY total ozone and NO₂ with the data of
890 ground-based UV-VIS measurements (m-124 and SAOZ), in *3rd Workshop on the*
891 *Atmospheric Chemistry Validation of Envisat (ACVE-3), ESRIN, Italy, 4-7 December*
892 *2006*, ESA SP-642, pp. —.

893 Kurucz, R. L., I. Furenlid, J. Brault, and L. Testerman (1984), *Solar flux atlas from*
894 *296 nm to 1300 nm*, vol. National Solar Observatory Atlas No. 1, National Solar
895 Observatory.

896 Lambert, J., M. Van Roozendaal, P. Simon, J. Pommereau, F. Goutail, J. Gleason,
897 S. Andersen, D. Arlander, N. Van, H. Claude, J. de la Noe, M. De Maziere,
898 V. Dorokhov, P. Eriksen, A. Green, K. Tornkvist, B. Hoiskar, E. Kyro, J. Leveau,
899 M. Merienne, G. Milinevsky, H. Roscoe, A. Sarkissian, J. Shanklin, J. Stahe-

900 lin, C. Tellefsen, and G. Vaughan (2001), Combined characterisation of GOME and
901 TOMS total ozone measurements from space using ground-based observations from
902 the NDSC, *Adv. Space Res.*, *26*(12), 1931–1940.

903 Levelt, P. F. and P. K. Bhartia (2007), Tbd, *J. Geophys. Res.*, *TBD*(TBD), doi:TBD,
904 TBD.

905 Levelt, P. F., E. Hilsenrath, G. W. Leppelmeier, G. H. J. van den Oord, P. K. Bhartia,
906 J. Taminnen, J. F. de Haan, and J. P. Veefkind (2006a), Science objectives of the
907 Ozone Monitoring Instrument, *IEEE Trans. Geosci. Rem. Sens.*, *44*(5), doi:10.1109/
908 TGRS.2006.872336, 1199–1208.

909 Levelt, P. F., G. H. J. van den Oord, M. R. Dobber, A. Malkki, H. Visser, J. de Vries,
910 P. Stammes, J. Lundell, and H. Saari (2006b), The Ozone Monitoring Instrument,
911 *IEEE Trans. Geosci. Rem. Sens.*, *44*(5), doi:10.1109/TGRS.2006.872333, 1093–1101.

912 Martin, R., C. Sioris, K. Chance, T. Ryerson, T. Bertram, P. Woolridge, R. Cohen,
913 J. Neuman, A. Swanson, and F. Flocke (2006), Evaluation of space-based constraints
914 on nitrogen oxide emissions with regional aircraft measurements over and downwind
915 of eastern north america, *J. Geophys. Res.*, *111*, doi:10.1029/2005JD006680.

916 Martin, R. V., D. J. Jacob, J. A. Logan, I. Bey, R. M. Yantosca, A. C. Staudt, Q. Li,
917 A. M. Fiore, B. N. Duncan, H. Liu, P. Ginoux, and V. Thouret (2002), Interpretation
918 of TOMS observations of tropical tropospheric ozone with a global model and in situ
919 observations, *J. Geophys. Res.*, *107*(D18), Article No. 4351.

920 Nizkorodov, S. A., S. P. Sander, and L. R. Brown (2004), Temperature and pressure
921 dependence of high-resolution air-broadened absorption cross sections of NO₂ (415–
922 525 nm), *J. Phys. Chem.*, *A108*, 4864–4872.

923 Piters, A., K. Bramstedt, J. Lambert, and B. Kirchhoff (2006), Overview of sciamachy
924 validation: 2002-2004, *Atmos. Chem. & Phys.*, *6*, 127–148.

925 Platt, U. (1994), *Chemical Analysis Series, 127, Differential optical absorption spec-*
926 *troscopy (DOAS), Air monitoring by spectroscopic techniques*, John Wiley & Sons,
927 Inc.

928 Russchenberg, H., F. Bosveld, D. Swart, H. ten Brink, G. de Leeuw, R. Uijlenhoet,
929 B. Arbesser-Rastburg, H. van der Marel, L. Ligthart, R. Boers, and A. Apituley
930 (2005), Groundbased atmospheric remote sensing in The Netherlands; European out-
931 look, *IEICE Transactions on Communications, E88-B(6)*, doi:10.1093/ietcom/e88-b.
932 6.2252, 2252–2258.

933 Spurr, R. J. D. (2001), Linearized radiative transfer theory: A general discrete ordi-
934 nate approach to the calculation of radiances and analytic weighting functions, with
935 application to atmospheric remote sensing, Ph.D. thesis, Technical University of Eind-
936 hoven, The Netherlands.

937 Spurr, R. J. D., T. P. Kurosu, and K. V. Chance (2001), A linearized discrete ordinate
938 radiative transfer model for atmospheric remote sensing retrieval, *J. Quant. Spectrosc.*
939 *Radiat. Transfer*, *68*, 689–735.

940 Thornton, J. A., P. J. Wooldridge, and R. C. Cohen (2000), Atmospheric NO₂: In
941 situ laser-induced fluorescence detection at parts per trillion mixing ratios, *Analytical*
942 *Chemistry*, *72*, 528–539.

943 Vandaele, A. C., C. Hermans, P. C. Simon, M. Carleer, R. Colin, S. Fally, M. F.
944 Mérienne, A. Jenouvrier, and B. Coquart (1998), Measurements of the NO₂ absorp-
945 tion cross-section from 42000 cm⁻¹ to 10000 cm⁻¹ (238–1000 nm) at 220 K and 294

946 K, *J. Quant. Spectrosc. Radiat. Transfer*, 59, 171–184.

947 Veefkind, J. P. and E. A. Celarier (2006), OMI level 2 NO₂ data product specifica-
948 tion, Tech. Rep. SD-OMIE-KNMI-352, KNMI and NASA Goddard Space Flight
949 Center. URL [http://disc.sci.gsfc.nasa.gov/Aura/OMI/OMN02_data_product_](http://disc.sci.gsfc.nasa.gov/Aura/OMI/OMN02_data_product_specification.pdf)
950 [specification.pdf](http://disc.sci.gsfc.nasa.gov/Aura/OMI/OMN02_data_product_specification.pdf).

951 Veefkind, J. P., E. J. Brinksma, K. F. Boersma, H. Eskes, J. F. Gleason, E. J. Bucsela,
952 E. A. Celarier, M. O. Wenig, and P. F. Levelt (2007), High spatial resolution NO₂
953 observations over europe using data from the ozone monitoring instrument, *Geophys.*
954 *Res. Lett.* (To appear.).

955 Wagner, T., B. Dix, C. v. Friedeburg, U. Frieß, S. Sanghavi, R. Sinreich, and U. Platt
956 (2004), MAX-DOAS O₄ measurements - a new technique to derive information on
957 atmospheric aerosols. (I) Principles and information content, *J. Geophys. Res.*, 109,
958 doi:10.1029/2004JD004904.

959 Wagner, T., J. Burrows, T. Deutschmann, B. Dix, F. Hendrick, C. von Friedeburg,
960 U. Frieß, K. Heue, H. Irie, H. Iwabuchi, Y. Kanaya, J. Keller, C. A. McLinden,
961 H. Oetjen, E. Palazzi, A. Petritoli, U. Platt, O. Postylyakov, J. Pukite, A. Richter,
962 M. van Roozendaal, A. Rozanov, V. Rozanov, R. Sinreich, S. Sanghavi, and F. Wit-
963 trock (2007), Comparison of Box-Air-Mass-Factors and Radiances for Multiple-Axis
964 Differential Optical Absorption Spectroscopy (MAX-DOAS) Geometries calculated
965 from different UV/visible Radiative Transfer Models, *Atm. Chem. Phys*, *accepted*.

966 Wittrock, F. (2006), *Dissertation: The retrieval of oxygenated volatile organic com-*
967 *pounds by remote sensing techniques*, University of Bremen.

968 Wittrock, F., H. Oetjen, A. Richter, S. Fietkau, T. Medeke, A. Rozanov, and J. P.
969 Burrows (2004), MAX-DOAS measurements of atmospheric trace gases in Ny-Ålesund
970 - Radiative transfer studies and their application, *Atmos. Chem. Phys.*, 4, 955–966.

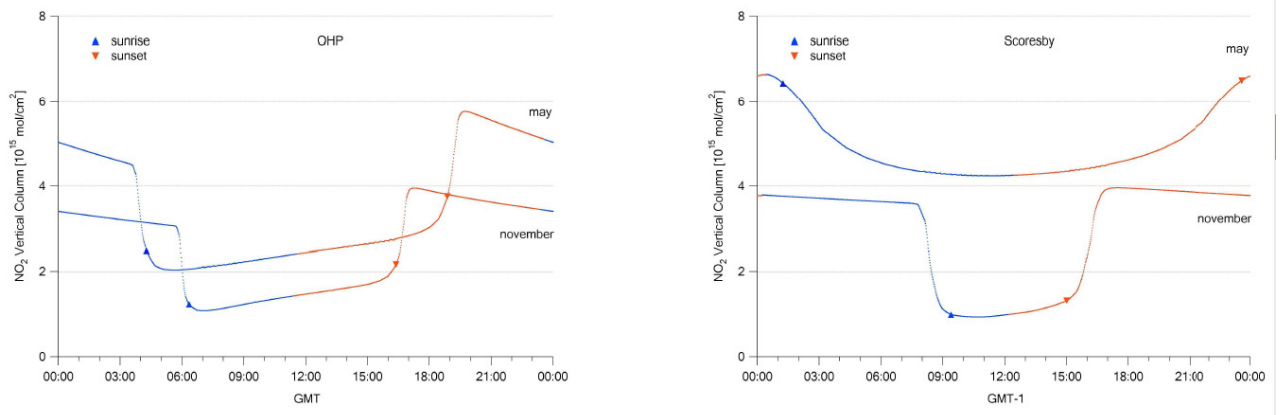


Figure 3. Simulated time-history of stratospheric NO₂ at a mid-latitude station (OHP), and a high-latitude station (Scoresbysund), for summer and winter.

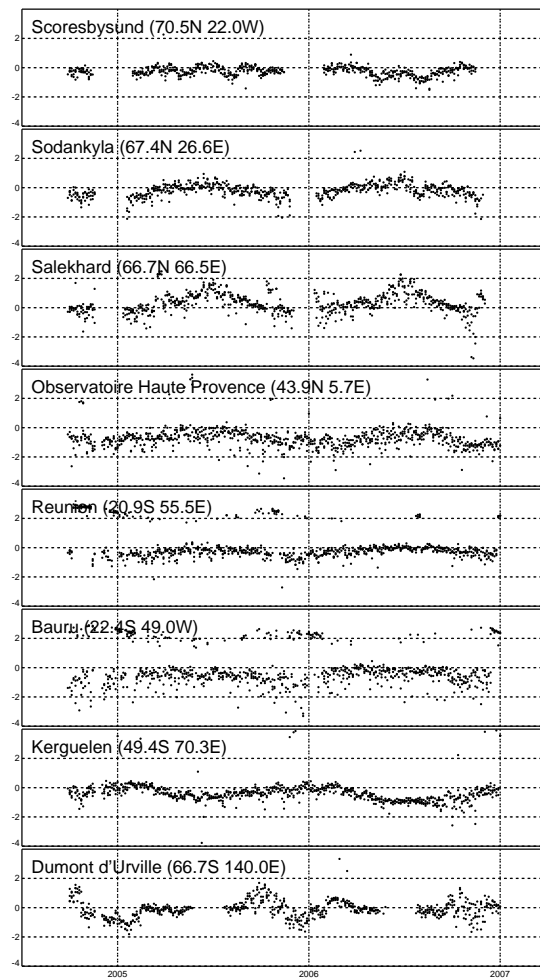


Figure 4. Time series of the difference between OMI and SAOZ-measured stratospheric NO_2 in units of 10^{15}cm^{-2} . The sites are ordered from North to South.

Table 1. Absolute average and r.m.s. difference (Δ , σ ; $\times 10^{16}$ cm $^{-2}$), and correlation (R) between ground-based SAOZ and satellite data, adjusted to sunrise OMI total and stratospheric NO $_2$ (2004-2005)

Station	SAOZ–OMI			SAOZ–OMI		
	total column			strat. column		
	Δ	σ	R	Δ	σ	R
Scoresby Sund	+0.09	0.82	0.92	-0.26	0.41	0.99
Sodankyla	+0.64	2.05	0.71	-0.22	0.54	0.97
Salekhard	+1.04	1.57	0.86	+0.25	0.74	0.97
OHP	+1.36	2.35	0.44	-0.83	1.04	0.67
Reunion	+0.29	0.77	0.29	-0.32	0.46	0.65
Bauru	+0.74	2.06	0.14	-0.65	0.86	0.56
Kerguelen	-0.12	0.61	0.87	-0.45	0.66	0.88
Dumont d’Urville	+0.37	1.17	0.87	-0.12	0.61	0.96
OVERALL:	+0.56	1.57	0.70	-0.34	0.70	0.91

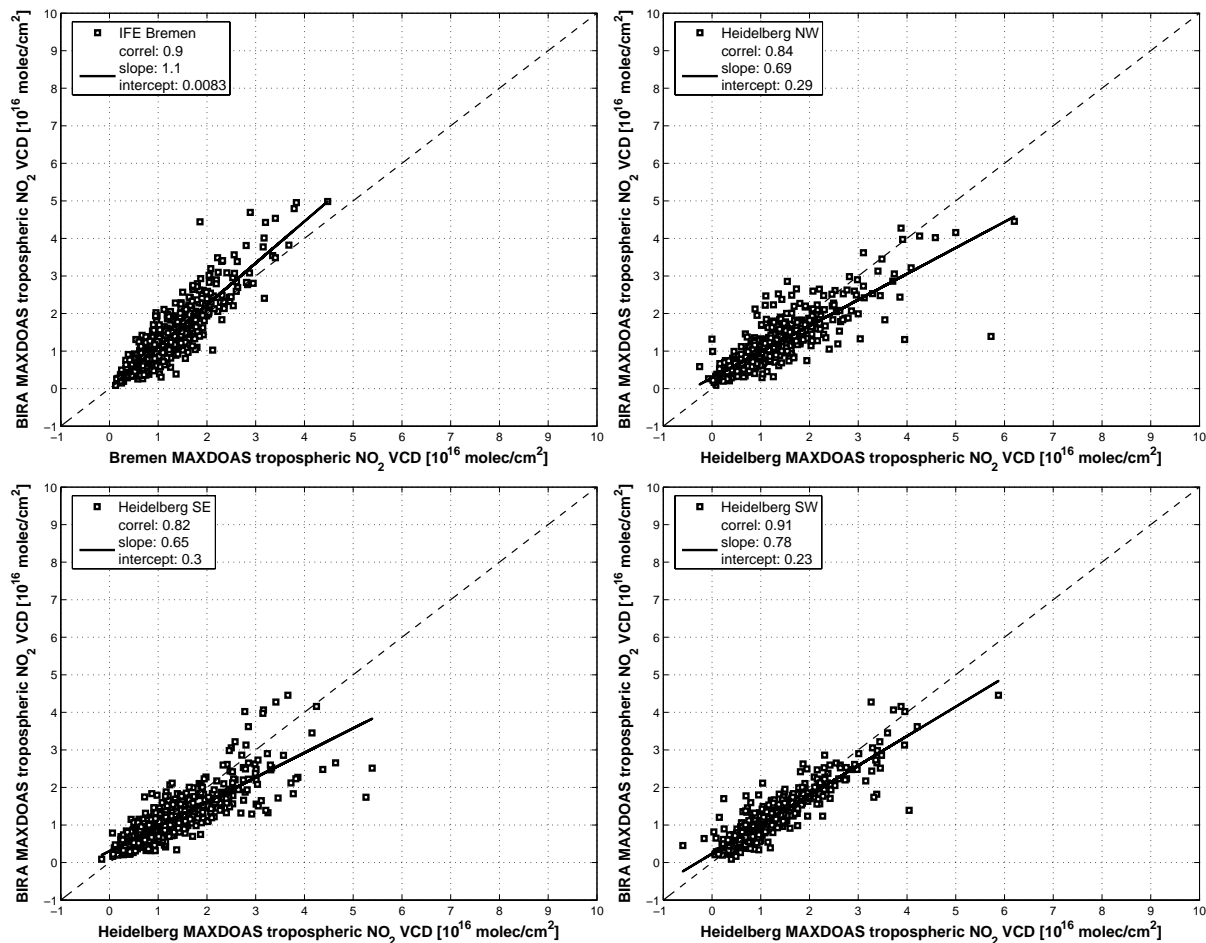


Figure 5. Scatter plots of the tropospheric NO₂ columns retrieved during the 2005 campaign from the BIRA MAX-DOAS instrument and, respectively, the Bremen MAX-DOAS (top left), the Heidelberg MAX-DOAS for the 3 pointing directions North-West (top right), South-East (bottom left) and South-West (bottom right). The regression analysis parameters are given in the legends. It has to be noted that agreement with the Heidelberg observations can be further improved after homogenisation of the retrieval settings (see text).

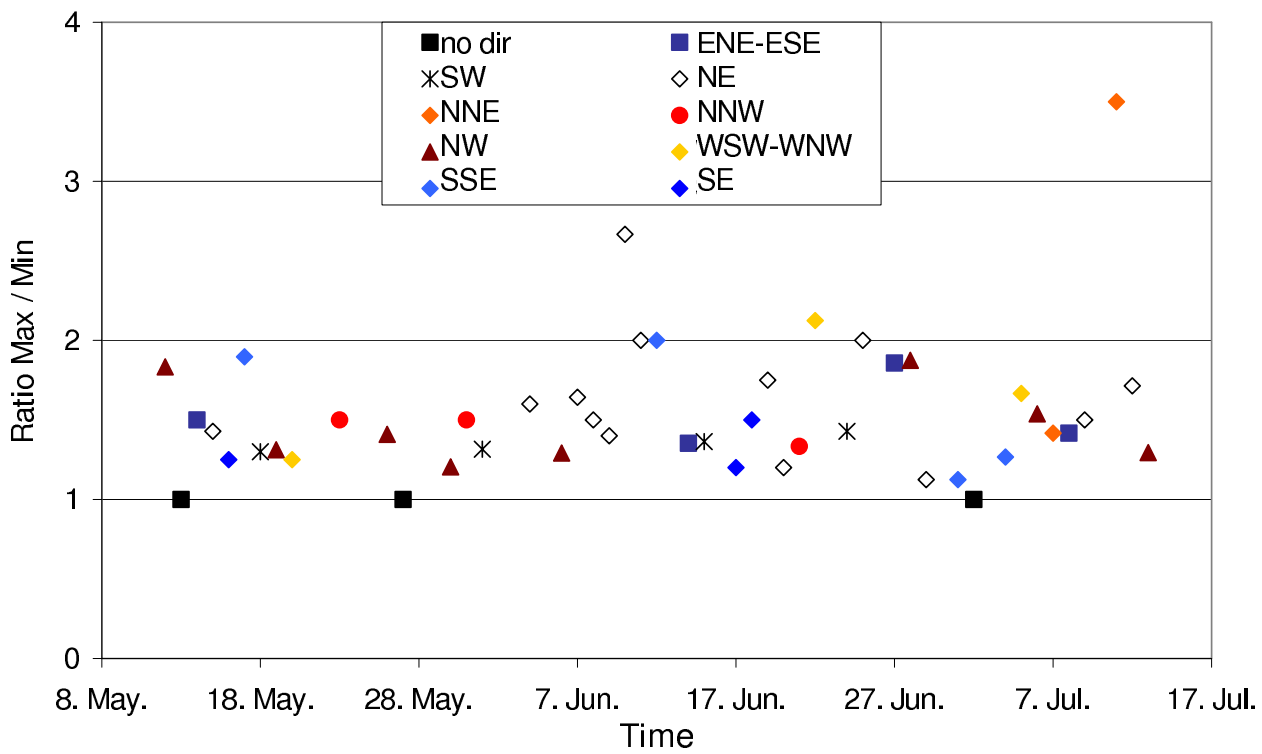


Figure 6. Maximum and minimum NO_2 SCD observed for an elevation angle of 3° of the Heidelberg MAX-DOAS telescopes observing under three different azimuth angles at Cabauw during the DANDELIONS campaign in 2005. High ratios indicate large horizontal gradients of the tropospheric NO_2 concentration field, colors indicate the direction of the gradient (directed toward higher values).

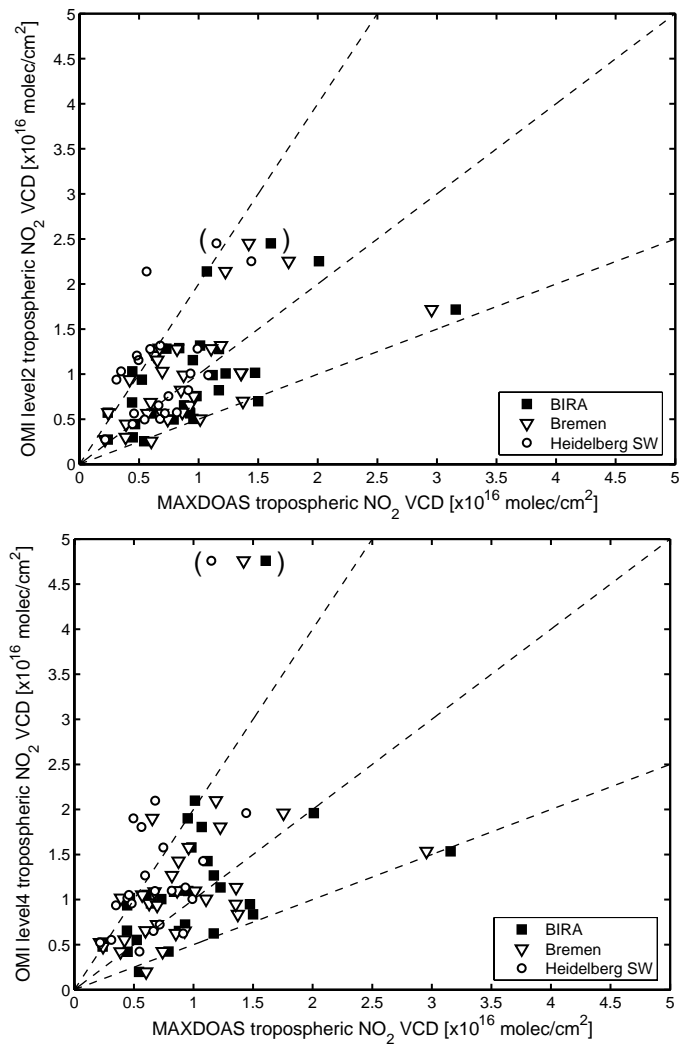


Figure 7. Correlations between tropospheric NO₂ from the three MAX-DOAS instruments at Cabauw (BIRA, Bremen, and Heidelberg SW direction) and OMI-L2 (top panel), or OMI-L4 (bottom panel). OMI data are included if cloud fractions were less than 20%. Correlation and regression coefficients are summarized in Table 2

Table 2. Statistical analysis of comparisons between tropospheric NO₂ from MAX-DOAS data and OMI (L2 and L4)

		BIRA					Bremen					
		South					South West					
	N	R	I	slope	rms	rms2	N	R	I	slope	rms	rms2
OMIL2	29	0.6	4.29	0.52	4.82	52%	29	0.63	3.93	0.59	4.44	48%
OMIL4	29	0.51	6.16	0.44	5.35	52%	29	0.52	5.99	0.48	5.18	50%

		Heidelberg					Heidelberg					
		South West					spatial average					
	N	R	I	slope	rms	rms2	N	R	I	slope	rms	rms2
OMIL2	21	0.45	4.27	0.8	5.38	56%	21	0.65	1.99	0.85	3.89	40%
OMIL4	21	0.39	6.84	0.67	6.50	57%	21	0.57	4.89	0.71	4.74	42%

^x N denotes number of collocations, R is Pearson correlation coefficient, I is intercept in units of $10^{15}m^{-2}$, slope denotes result of linear regression analysis, rms denotes rms difference between groundbased and OMI, in units of $10^{15}m^{-2}$, and rms2 denotes the same in percent relative to the average OMI value.

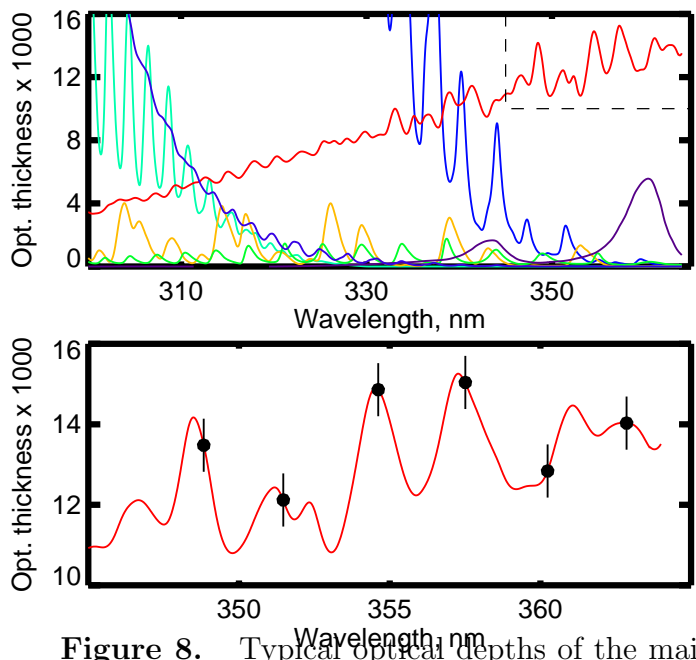


Figure 8. Typical optical depths of the main trace gases in the Brewer MK-III wavelength range. Lower: NO₂ optical depth for 1 DU ($= 2.7 \times 10^{16} \text{ cm}^{-2}$), 6 slit positions with noise estimates.

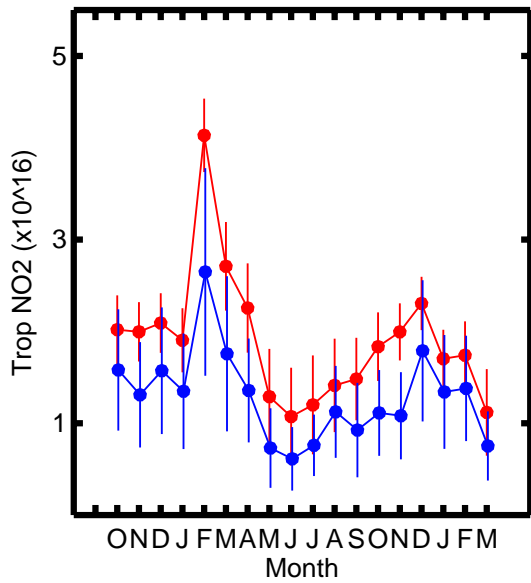


Figure 9. Comparison between the monthly mean Brewer-measured and OMI-measured NO_2 total columns.

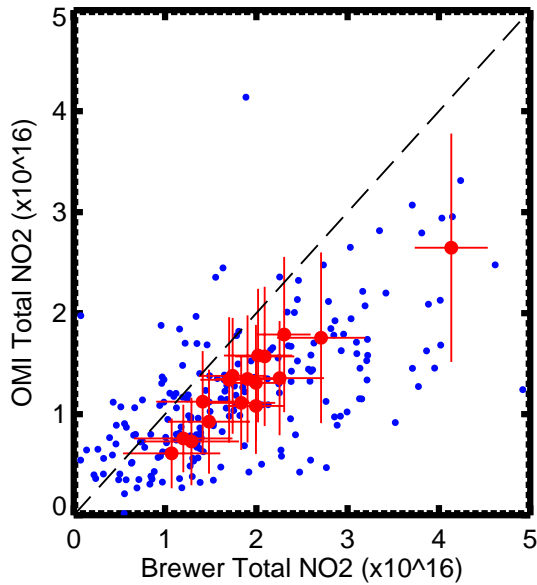


Figure 10. Daily mean and monthly mean values of NO_2 total column measured by the Brewer instrument and OMI. The line of linear regression is also shown.

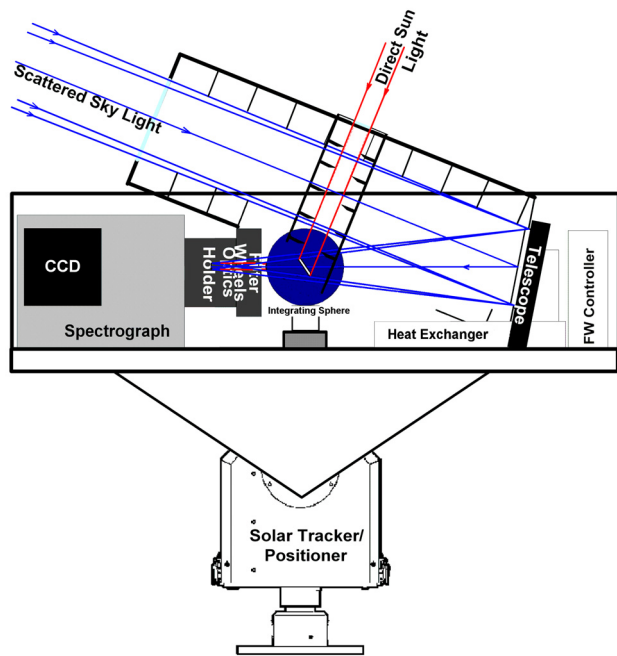


Figure 11. Schematic drawing of the MF-DOAS instrument.

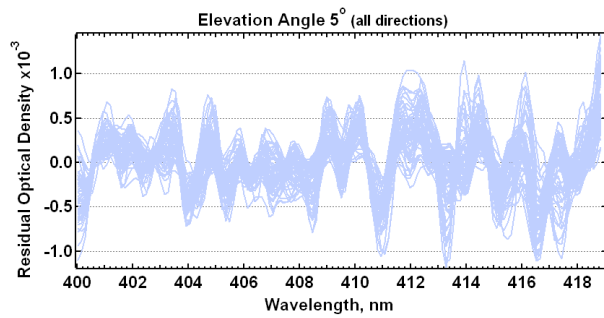


Figure 12. Representative residual optical densities for observations of May 9, 2006 at 5° elevation and 4 azimuth angles.

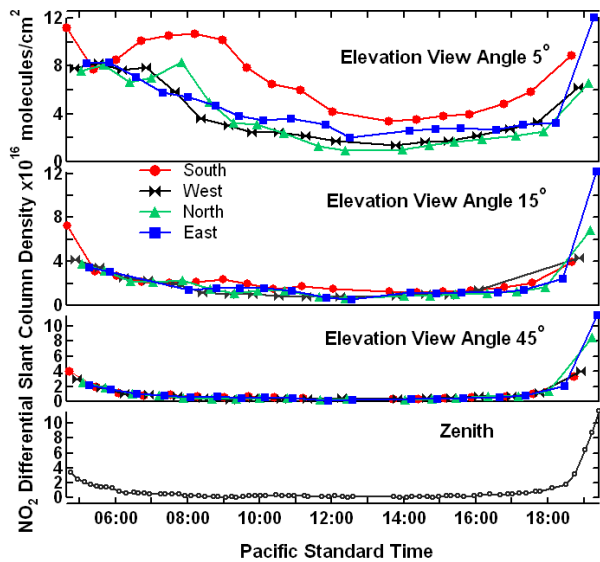


Figure 13. Example of measured spatial and temporal variation of MF-DOAS-measured NO_2 differential SCD for May 9, 2006

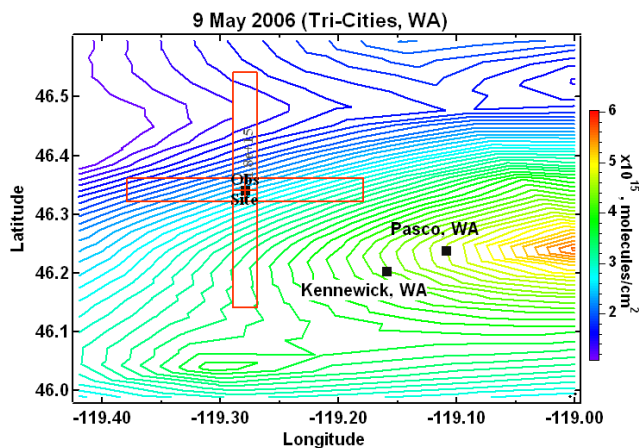


Figure 14. Tropospheric NO_2 VCD over the Tri-Cities area of Washington State on May 9, 2006. The contour map is derived from the individual OMI FOV measurements.

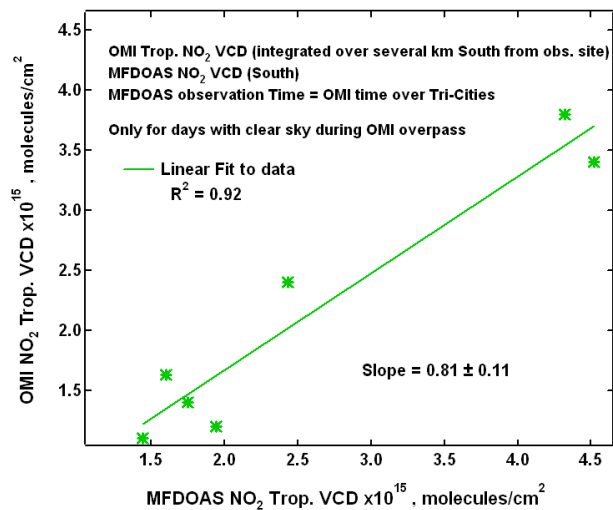


Figure 15. Correlation between OMI tropospheric NO₂ vertical column and MF-DOAS NO₂ tropospheric vcd for measurements made from April 30 through May 13, 2006

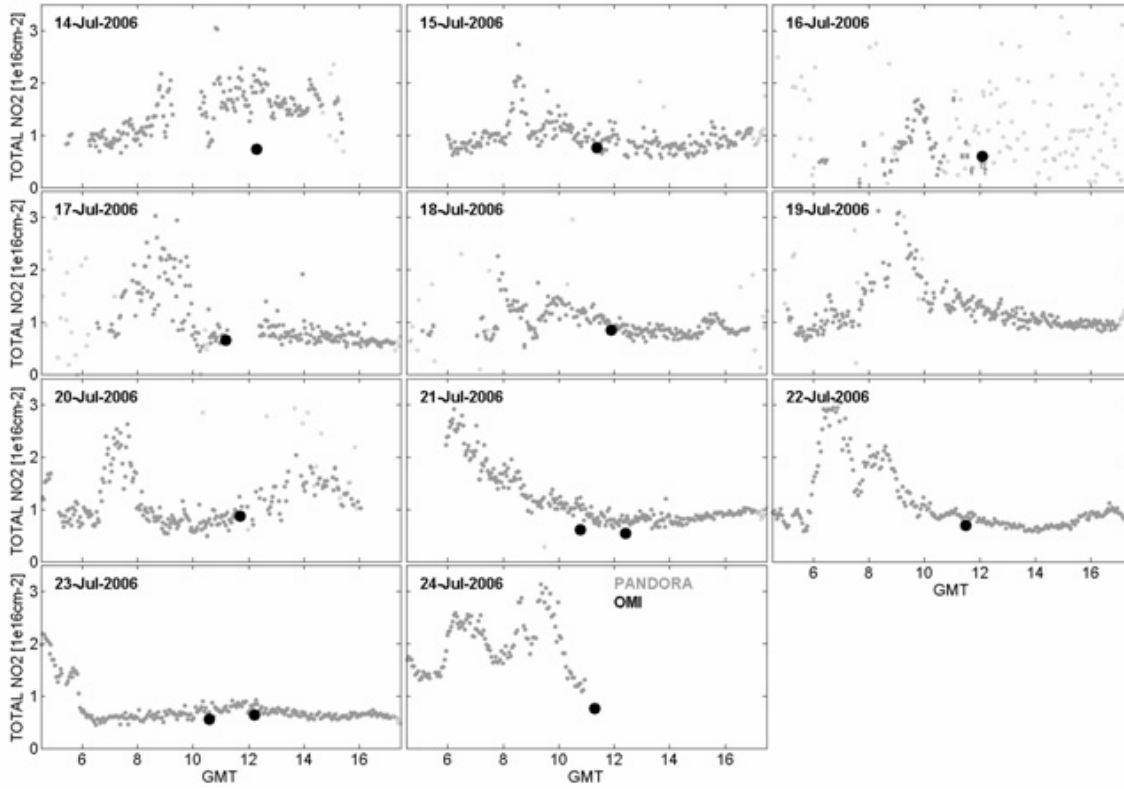


Figure 16. Pandora-1 Data measured during the period 14–24 July 2006, in Thessaloniki (grey dots) and OMI overpass data for the site (large black dots).

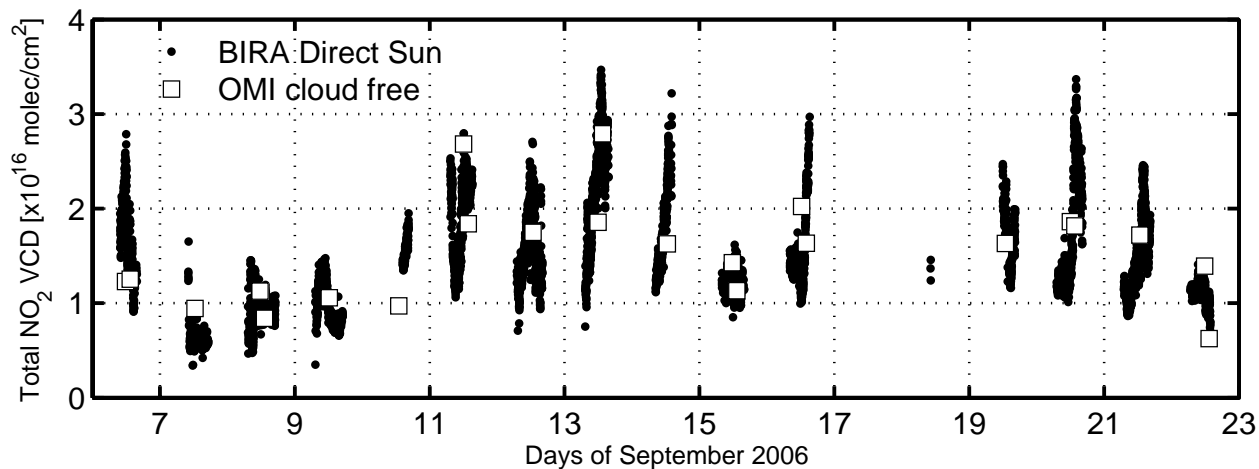


Figure 17. Time series of NO₂ VCD measured by the BIRA direct-sun DOAS instrument.

The open squares show the collocated OMI measurements.

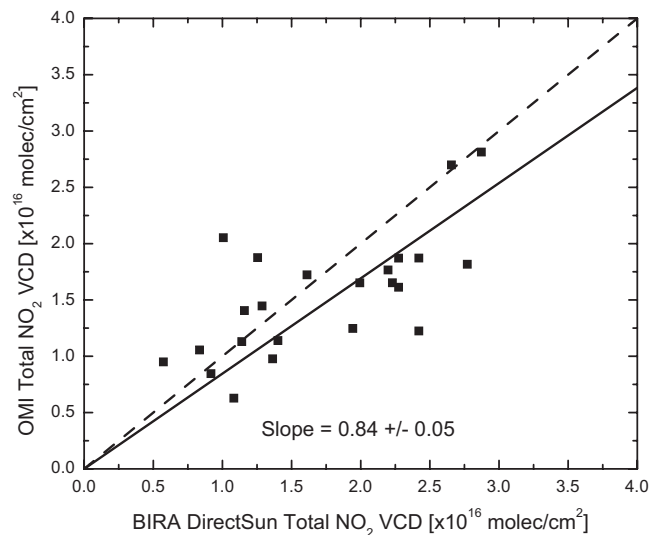


Figure 18. Correlation plot showing the collocated OMI and BIRA direct-sun DOAS instrument measurements (open squares in Figure 17).

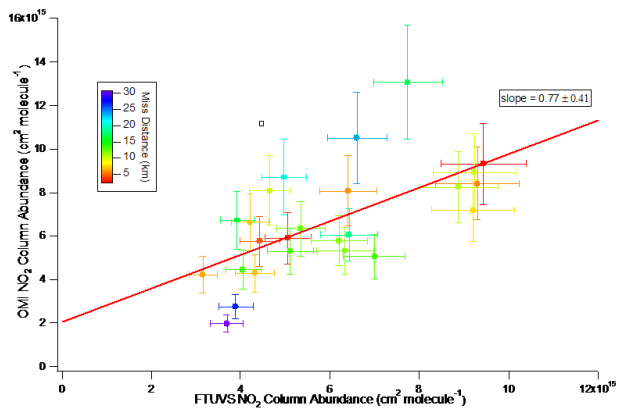


Figure 19. OMI versus FTUVS measurements of total column NO₂, binned by distance between TMF and the centroid of the OMI FOV (distance indicated by color, see inset scale)

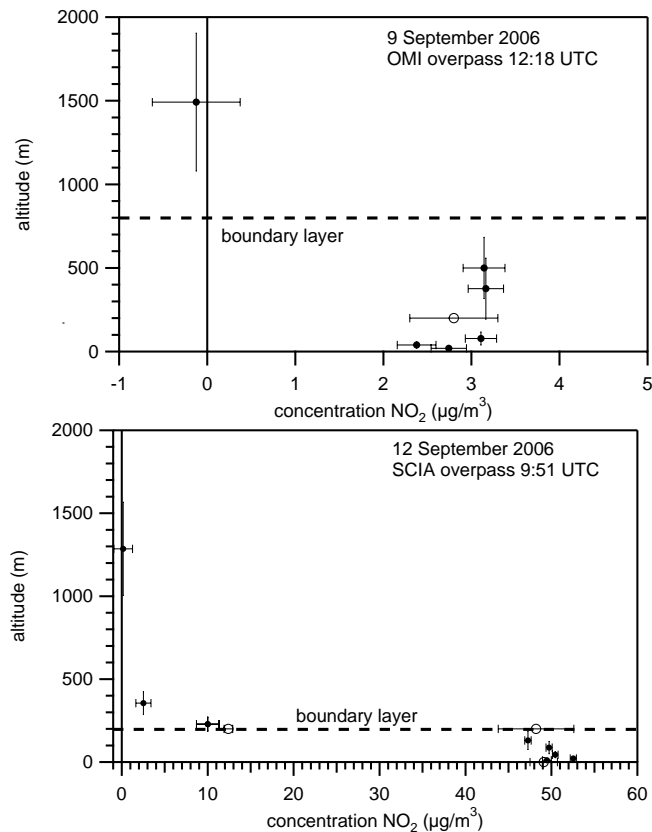


Figure 20. Lidar NO₂ profile (black circles) and NO₂ monitor value (open circle) measured at Cabauw. Horizontal bars indicate two-sigma values for the concentration. For the lidar data, vertical bars indicate the height intervals over which concentrations have been determined. The boundary layer height is indicated by a dashed line. Top panel: Clean day, September 9, 2006 (lidar measurement from 12:04–12:52 UT). On this day, the NO₂ monitor at ground level was not operational. NO₂ monitor data at 200 m were averaged over the lidar integration time. Bottom panel: Polluted day, September 12, 2006 (lidar measurement from 9:37–10:26 UT). For the NO₂ monitor data at ground level an average was made for the time the monitor was operational during this interval, from 10:03–10:17. For the data of the NO₂ monitor at 200 m two averages were determined; the lower average, for 9:37–10:17 UT, is for the situation that the NO₂ monitor is above the boundary layer, the higher value, for 10:16–10:26 UT, is for the situation that the NO₂ monitor is situated below the boundary layer.

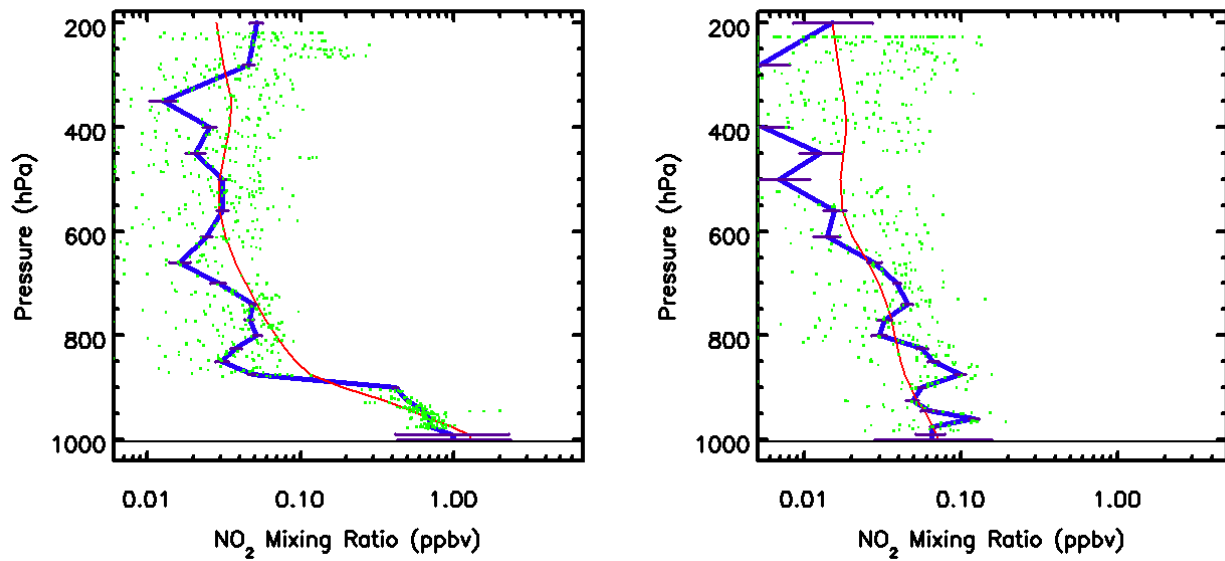


Figure 21. Two INTEX-B NO₂ profiles. The upper panel shows data for a profile measured over the Mississippi-Alabama border (32.0 N, 88.3 W), while the lower panel shows data for a profile measured over the Gulf of Mexico (23.0 N, 91.1 W). Green dots are original measurements, the blue line is binned profile, and the red line is the annual mean GEOS-CHEM model profile for that location.

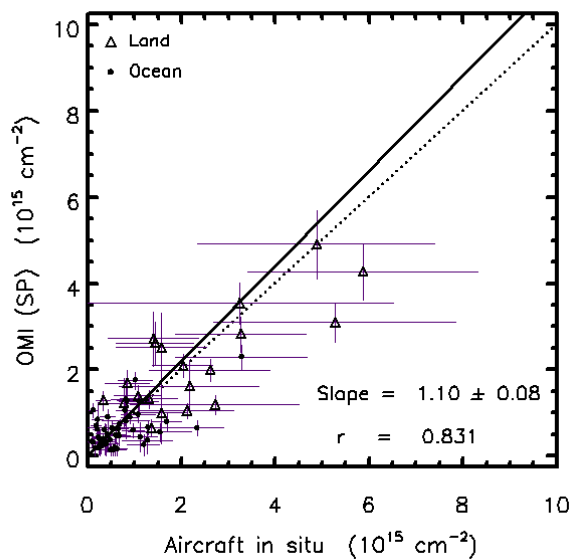


Figure 22. Tropospheric NO₂ columns with *in situ* columns from INTEX-B. The symbols indicate land measurements (triangle) or ocean measurements (dot). The dotted line is a 1:1 ratio and the solid line is the fit to the data.

Table 3. Summary of validation study results for OMI NO₂ data product.

Instrument	Column	Group	OMI, rel. to GB	Remarks
SAOZ	Strat.	CNRS	+10%	As large as 50% in tropics.
MAX-DOAS	Trop.	BIRA, etc.	-15%	Large scatter in the data.
Brewer	Total	GSFC	-33%	Large N , large scatter.
MF-DOAS	Total	WSU	-19%	Very small N .
Pandora-1	Total	GSFC	-15%	Very small N .
DS-DOAS	Total	BIRA	-16%	Small N , large scatter.
FTUVS	Total	JPL	-23%	Small N , but good correlation.
Aircraft <i>in situ</i>	Trop.	UC Berkeley, GSFC	+10%	Large scatter.
